

TECHNICAL REPORT STANDARD TITLE PAGE

1. Report No. ATC-176	2. Government Accession No. DOT/FAA/NR-90/5	3. Recipient's Catalog No.	
4. Title and Subtitle A Study of Dry Microburst Detection with Airport Surveillance Radars		5. Report Date 29 November 1990	
		6. Performing Organization Code	
7. Author(s) Mark A. Meister		8. Performing Organization Report No. ATC-176	
9. Performing Organization Name and Address Lincoln Laboratory, MIT P.O. Box 73 Lexington, MA 02173-9108		10. Work Unit No. (TRAIS)	
		11. Contract or Grant No. DTFA-01-L-83-4-10579	
12. Sponsoring Agency Name and Address Department of Transportation Federal Aviation Administration Systems Research and Development Service Washington, DC 20591		13. Type of Report and Period Covered Project Report	
		14. Sponsoring Agency Code	
15. Supplementary Notes This report is based on studies performed at Lincoln Laboratory, a center for research operated by Massachusetts Institute of Technology under Air Force Contract F19628-90-C-0002.			
16. Abstract This report evaluates the capability of Airport Surveillance Radars (ASRs) for the detection of low altitude wind shear associated with the outflows of dry microbursts. It describes results of simulations of dry microburst observations by an ASR. These simulations incorporated weather and clutter data collected by the FL-2 pencil-beam Doppler weather radar at Denver Stapleton Airport in 1988 and 1989 and clutter data collected by the FL-3 ASR-9 emulation radar at Huntsville, Alabama. The impact of signal strength, overhanging precipitation, and ground clutter on both observability and algorithmic performance are assessed. Principal results of study are the following: 1. Overhanging precipitation and weak signal strength do not, by themselves, prohibit detection of dry outflows; however, occurrence of false alarms and biases in velocity estimates indicate that improvements in the dual beam estimator that was evaluated would be required for reliable detection of these events. 2. Ground clutter tends to obscure dry outflows in regions where the difference between median effective clutter reflectivity and weather reflectivity exceeds 17-20 dB. A method for predicting the percentage of missed microburst detections due to ground clutter is used to estimate overall microburst detection probabilities for a "dry" environment such as Denver. Using measured clutter from an experimental ASR in Huntsville, AL, overall microburst detection probability is 83 percent. Using simulated Denver clutter, overall detection probability is 91 percent.			
17. Key Words airport surveillance radar dry microburst detection simulation		18. Distribution Statement Document is available to the public through the National Technical Information Service, Springfield, VA 22161.	
19. Security Classif. (of this report) Unclassified	20. Security Classif. (of this page) Unclassified	21. No. of Pages 78	22. Price

ABSTRACT

This report evaluates the capability of Airport Surveillance Radars (ASRs) for the detection of low altitude wind shear associated with the outflows of dry microbursts. It describes results of simulations of dry microburst observations by an ASR. These simulations incorporated weather and clutter data collected by the FL-2 pencil-beam Doppler weather radar at Denver Stapleton Airport in 1988 and 1989 and clutter data collected by the FL-3 ASR-9 emulation radar at Huntsville, Alabama. The impact of signal strength, overhanging precipitation, and ground clutter on both observability and algorithmic performance are assessed.

Principal results of study are the following:

1. Overhanging precipitation and weak signal strength do not, by themselves, prohibit detection of dry outflows; however, occurrence of false alarms and biases in velocity estimates indicate that improvements in the dual beam estimator that was evaluated would be required for reliable detection of these events.
2. Ground clutter tends to obscure dry outflows in regions where the difference between median effective clutter reflectivity and weather reflectivity exceeds 17-20 dB.

A method for predicting the percentage of missed microburst detections due to ground clutter is used to estimate overall microburst detection probabilities for a "dry" environment such as Denver. Using measured clutter from an experimental ASR in Huntsville, AL, overall microburst detection probability is 83 percent. Using simulated Denver clutter, overall detection probability is 91 percent.

Accession For	
NTIS GRA&I	<input checked="checked" type="checkbox"/>
DTIC TAB	<input type="checkbox"/>
Unannounced	<input type="checkbox"/>
Justification	
By	
Distribution/	
Availability Codes	
Dist	Avail and/or Special
A-1	

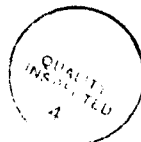


TABLE OF CONTENTS

<u>Section</u>	<u>Page</u>
Abstract	iii
List of Figures	vii
List of Tables	viii
1. INTRODUCTION	1
A. Radar Sensitivity	1
B. Overhang Precipitation Interference	2
C. Clutter Residue Interference	3
2. EXPERIMENTAL PROCEDURE	5
A. Case Selection	6
B. Generating Fan-Beam Time-Series from Pencil-Beam Products	7
C. Generating Clutter Time-Series from Pencil-Beam and Fan-Beam Data	9
D. Signal Processing: Generating ASR Weather Products	15
E. Microburst Detection Algorithm	16
3. RESULTS	17
A. Case Studies	17
B. Effects of Signal-to-Noise and Overhanging Precipitation on Dry Microburst Detection	53
C. Effects of Clutter Residue on Dry Microburst Detection	54
D. False Alarms and Other Issues	59
4. CONCLUSION	63
REFERENCES	65
APPENDIX A - Synthesis of RHIs from PPI Volume Scan Data	67

LIST OF FIGURES

<u>Figure No.</u>	<u>Page</u>
1. Minimum and maximum detectable reflectivity versus range for an ASR-9	2
2. Dry microburst simulation and processing block diagram	6
3. ASR-9 weather and clutter simulation block diagram	8
4. Median ground clutter intensity (ensembled over azimuth) versus range: a) from the ASR-8 at Stapleton Airport (from Weber, 1987); b) from coordinate-translated FL-2 data	12
5. Clutter maps used in dry microburst study, in units of weather reflectivity (dBZ)	13
6. FL-2 pencil-beam reflectivity and radial velocity fields during 5 dBZ dry microburst at 8 km, 316 degrees azimuth, at 20:41 (GMT), August 8, 1988 in Denver	19
7. Vertical profile of 20:41 (GMT), August 8, 1988 dry microburst event	21
8. Simulated ASR reflectivity and velocity fields for 20:41 (GMT), August 8, 1988 dry microburst event	23
9. Simulated clutter-contaminated ASR velocity fields for 20:41 (GMT), August 8, 1988 dry microburst event	25
10. FL-2 pencil-beam reflectivity and radial velocity fields during 15 dBZ dry microburst at 6 km, 219 degrees azimuth at 23:07 (GMT), June 12, 1987 in Denver	29
11. Vertical profile of 23:07 (GMT), June 12, 1987 dry microburst event	31
12. Simulated ASR velocity fields for June 12, 1987 dry microburst event	33
13. FL-2 pencil-beam reflectivity and radial velocity fields during 10 dBZ dry microburst at 13 km, 265 degrees azimuth at 22:10 (GMT), June 10, 1988 in Denver	35
14. Vertical profile of 22:10 (GMT) June 10, 1988 dry microburst event	37
15. Vertical profile of 22:10 (GMT) June 10, 1988 dry microburst event	41
16. Simulated ASR velocity fields for 22:10 (GMT) June 10, 1988 dry microburst event	43

LIST OF FIGURES (Continued)

<u>Figure No.</u>	<u>Page</u>
17. FL-2 pencil-beam reflectivity and radial velocity fields during 5 dBZ dry microburst at 12 km, 256 degrees azimuth at 23:19 (GMT) June 10, 1988 in Denver	45
18. Vertical profile of 23:19 (GMT) June 10, 1988 dry microburst event	47
19. Simulated ASR velocity fields for 22:10 (GMT) June 10, 1988 dry microburst event	49
20. Simulated ASR velocity fields for 22:10 (GMT) June 10, 1988 dry microburst event	51
21. Algorithmic hits (Xs) and misses (boxes) from LBV and DBV fields with adjusted signal-to-noise and signal-to-clutter thresholds plotted on a graph of effective clutter reflectivity versus weather reflectivity	56
22. Histogram of microburst surface reflectivity for Denver microburst events exceeding 20 meters per second	57
23. Histograms of clutter intensity (in units of effective clutter reflectivity) for a) Denver and b) Huntsville for range interval 0-15 km	58
A-1. Cressman weight versus relative distance for four values of alpha	68

LIST OF TABLES

<u>Table No.</u>	<u>Page</u>
1. Dry Microburst Events in Study	7
2. ASR Simulated Radar Parameters	10
3. Clear Day Clutter Map Attenuation Factors	12
4. Scoring Results, Pure Weather (11 Cases)	53
5. Microburst Detection Algorithm Velocity Estimator Performance for Simulated ASR-based Dry Microburst Velocity Fields Generated Using Dual-Beam Autocorrelation Method	54
6. Weather Plus Clutter Scoring Results (11 Cases - DBV)	55
7. False Association Scoring Results (11 Cases)	61

1. INTRODUCTION

This report considers the capability of Airport Surveillance Radars (ASRs) for detecting the low altitude wind shear associated with the outflows of dry microbursts. It describes results of simulations of dry microburst observations by an ASR. These simulations incorporated weather and clutter data collected by Lincoln Laboratory's Terminal Doppler Weather Radar testbed (FL-2) at Denver Stapleton Airport in 1988 and 1989 and clutter data collected by Lincoln Laboratory's ASR-9 emulation testbed (FL-3) at Huntsville, Alabama. The impact of signal strength, overhanging precipitation, and ground clutter on both radar observability and algorithmic performance are assessed.

Field studies in Huntsville have shown that ASRs can adequately detect wind shear hazards in "wet" meteorological environments (Weber and Noyes, 1988). This is important, since wet microbursts are by far the predominant source of low altitude wind shear at most of the potential ASR-9 sites in the United States.

Wet microbursts occur in regions where the low altitude relative humidity is high; as a result, the height of the ambient cloudbase is low (typically one km above ground level) and evaporation of precipitation accompanying a convective storm's downdraft is negligible. Such microbursts, always associated with a moderate to intense rainfall on the ground, are designated "wet" microbursts. However, at some potential ASR-9 sites (e.g., the Great Plains and the deserts east of the Rocky Mountains), dry microbursts, events associated with much lower reflectivity convective storms, occur. In these drier regions, the cloud base can often be as high as 3 km above ground level. Under these conditions, convective storms still develop, generating strong downdrafts. Much of the precipitation accompanying these downdrafts evaporates before reaching the ground. A resultant outflow can therefore be very dry, and the signal returned to a weather radar detection system correspondingly low. In Denver, during the months of high microburst activity (May to September), a deep boundary layer of dry air exists roughly half the time. During field experiments conducted at Denver's Stapleton Airport over the summers of 1987 and 1988, 41 percent of the microburst events observed by the FL-2 radar were associated with reflectivities of 30 dBZ or less, technically classifying them as dry. Many dry microburst downdrafts are associated with the anvils of larger "wetter" convective storms located tens of kilometers away.

Both the ambient cloud structure and the low surface reflectivity associated with dry microbursts impose technical challenges peculiar to an ASR-based wind shear detection system. These challenges can be divided into three categories: radar sensitivity, overhang precipitation interference, and ground clutter interference.

A. RADAR SENSITIVITY

Dry microbursts can exhibit surface reflectivities as low as 5 dBZ. While the ASR-9 radar is inherently capable of detecting signals below 0 dBZ as far out in range as 23 km, operation at maximum sensitivity is impractical on account of receiver clipping caused by saturation from both high ground clutter and severe weather. The 12-bit analog-to-digital converters of the ASR-9 receiver impose a 66 dB dynamic range on the system. To counter receiver saturation, the sensitivity of the system is currently reduced at close ranges by applying a range-dependent Sensitivity Time Control (STC) function. Figure 1 plots both minimum detectable signal and saturation point versus range in units of reflectivity for the ASR-9. The dotted curve shows the receiver with no STC. The

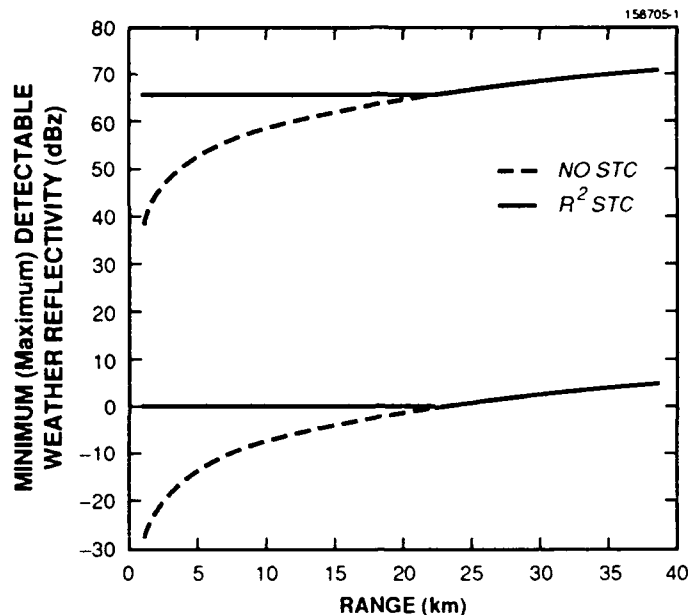


Figure 1. Minimum and maximum detectable reflectivity versus range for an ASR-9. Dashed curve shows sensitivity and saturation limits with STC switched off. Solid curve shows limits with range squared STC function.

solid curve shows sensitivity after applying an STC function that varies as the square of the range. This function was so selected to give a constant sensitivity of 0 dBZ out to 23 km. Weber and Moser (1987) have shown that such an STC function should provide the ASR-9 with adequate protection from receiver saturation in typical clutter environments.

The use of an IAGC system as an alternative to the STC is currently under investigation. This would effectively broaden the dynamic range, affording both higher sensitivity and a higher saturation point. Such a system improvement will be implemented on an ASR-9 transportable testbed in late 1990.

B. OVERHANG PRECIPITATION INTERFERENCE

An ASR fan-beam pattern would not only receive echoes from the low elevation outflow, but also from the storm above the outflow, biasing Doppler estimates of near surface wind velocity. Weber and Noyes (1988) and Weber (1989) have shown this to be a solvable problem in the case of wet microbursts within 20 km of the radar. However, for dry microbursts, this overhanging precipitation interference would be much more acute, since evaporation causes a decrease in the ratio of echo strength from the low elevation outflow region to echo strength from aloft.

C. CLUTTER RESIDUE INTERFERENCE

Weber (1988) has performed simulations indicating that typical levels of ground clutter for an ASR would not prevent detection of microburst outflows with reflectivity in excess of 20 dBZ. However, dry microbursts can return echoes as low as 5 dBZ. Typical signal-to-clutter ratios in event regions often will be less than -25 dB; clutter residue and/or clutter filtering may seriously distort the weather echo spectrum.

Since 1985, the FAA and Lincoln Laboratory have conducted a multi-year study, FLOWS (FAA/Lincoln Laboratory Operational Wind Shear Studies), to assess the wind-shear detection capabilities of Doppler weather radars sited at or near airports. The primary weather radar used in these studies is an S-band pencil-beam weather radar (FL-2). Data have been collected from four sites thus far: Memphis, TN (1985), Huntsville, AL (1986), Denver, CO (1987-88), and Kansas City, KS (1989). Since no testbed ASR Doppler weather data has been collected in a dry microburst environment and a large quantity of pencil-beam dry microburst data collected by FL-2 in Denver was available, the FL-2 Denver data set was used in simulations to assess an ASR-9s dry microburst detection capability.

The breakdown of the report is as follows: Section 2 describes in detail the procedure followed in the assessment. The criteria used in the selection of 11 dry microburst cases are discussed. Techniques used in simulating time-series signals corresponding to an ASR's measurements of dry microbursts and competing ground clutter are described. The section concludes by describing subsequent Doppler signal processing and application of the microburst detection algorithm. Section 3 presents the results of the simulation and the analysis of the eleven microburst cases. Each of the three above mentioned detection issues, radar sensitivity, overhanging precipitation, and clutter residue is addressed. In section 4, conclusions and recommendations are given.

2. EXPERIMENTAL PROCEDURE

Eleven dry microbursts events were selected from FL-2 data for study. The block diagram in Figure 2 depicts the scheme used in processing them. In brief:

1. FL-2 volume scan weather reflectivity, radial velocity, and spectral width data were used to compute elevation-angle resolved spectra of weather echoes. These were weighted by the beam pattern of the ASR-9, then integrated over beam elevation.
2. An additional signal component simulating system noise was applied to the composite spectra from step 1). The Monte Carlo method described by Sirmans and Bumgarner (1975) was then used to simulate Rayleigh amplitude statistics and a uniform random phase distribution for each spectral component.
3. The resultant "noisy" composite spectral data were inverse Fourier transformed to time-series.
4. Clutter time-series were generated from clear day clutter data collected from both the FL-2 (Denver) and FL-3 (Huntsville) radar systems. These clutter time-series were added to the weather time-series generated in step 3).
5. Both pure weather time-series from step 3) and clutter-contaminated weather time-series from step 4) were converted to reflectivity and radial velocity products using the ASR signal processing algorithms currently employed by the FL-3 real-time signal processor.
6. Wind shear segment associations, clusters, were generated from the product data using a slightly modified version of the divergent outflow detection algorithm developed for TDWR.
7. Both product data from step 5 and cluster data from step 6 were analyzed.

This chapter details the case selection and the processing scheme used in the first five steps above. Included are:

1. The selection criteria for the 11 dry microburst cases studied;
2. Methods used to simulate ASR fan-beam time-series data from FL-2 pencil-beam volume scan weather data;
3. The conversion of FL-2 and FL-3 clutter data to ASR time-series format;
4. The time-series ASR signal processor used to generate low-altitude radial velocity estimates, and the application of the microburst detection algorithm.

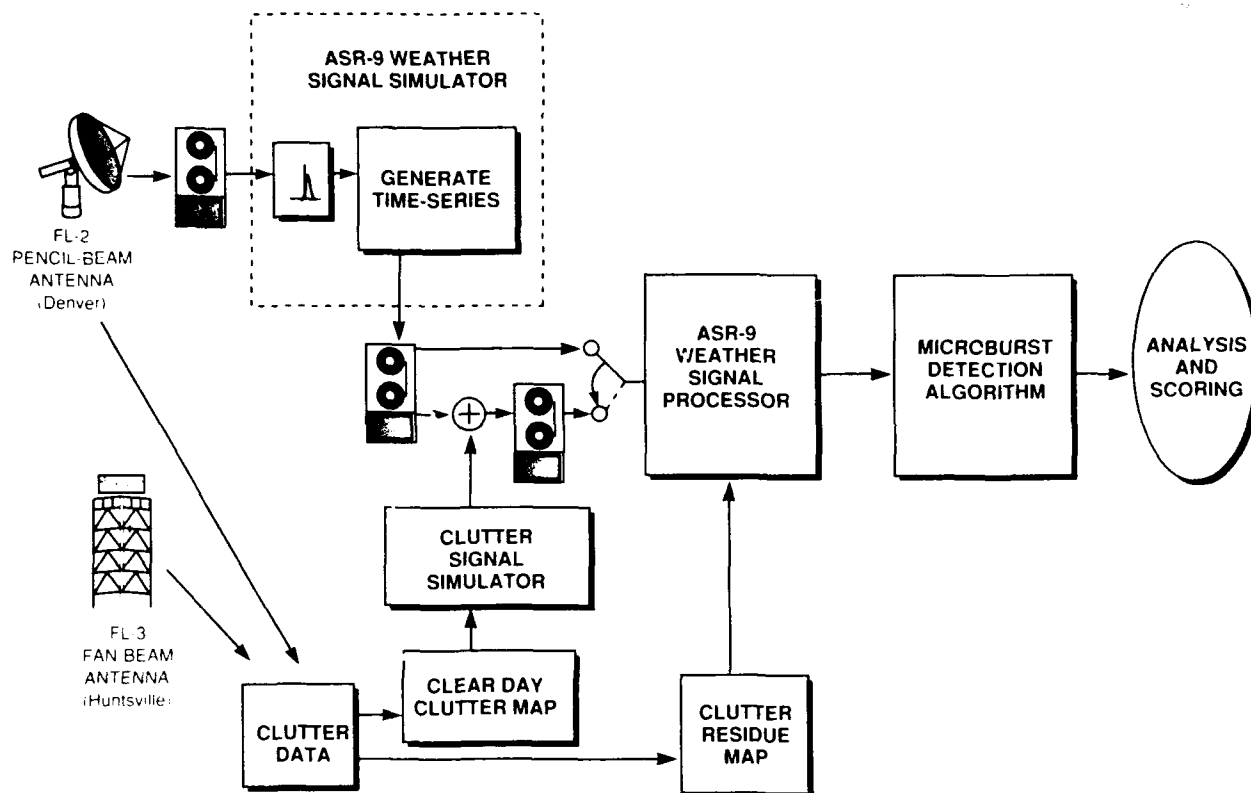


Figure 2. Dry microburst simulation and processing block diagram.

A. CASE SELECTION

Eleven dry microburst volume scans were selected from FL-2 Denver 1987 and 1988 data. The three criteria used in choosing the events were:

1. a maximum wind shear exceeding 20 m/sec;
2. the event center no farther than 15 km from the radar; and
3. the peak reflectivity in the neighborhood of the event during maximum shear less than 20 dBZ.

Table 1 lists 11 Denver microburst cases which met these criteria. Listed are time, magnitude of peak differential velocity, maximum local reflectivity, and location of the event's center, as measured by the FL-2 pencil-beam weather radar.

Table 1.
Dry Microburst Events in Study

Case Number	Date	Time (GMT)	Shear (m/s)	Reflectivity (dBZ)	Range (km)	Azimuth (degrees)
1	12 June 1987	23:07	24	15	6	219
2	18 June 1987	22:36	21	15	14	255
3	10 July 1987	00:54	30	10	7	311
4	10 July 1987	01:44	28	10	13	198
5	10 July 1987	01:52	27	10	3	193
6	10 June 1988	22:10	27	10	13	265
7	10 June 1988	23:19	24	5	12	256
8	8 August 1988	20:41	22	5	6	316
9	9 August 1988	19:37	22	15	14	330
10	12 August 1988	22:04	22	15	14	289
11	12 August 1988	22:29	24	10	7	307

B. GENERATING FAN-BEAM TIME-SERIES FROM PENCIL-BEAM PRODUCTS

This section describes the method used to simulate fan-beam ASR time-series from pencil-beam FL-2 volume scan data. The FL-2 volume scan data used for each event studied consisted of 7-14 PPI scans of product data. Three products were used: reflectivity (DZ), velocity (V), and spectrum width (SW). The time of the lowest level tilt, i.e., the surface scan, was the time of maximum observed shear. The remaining tilts were selected such that the surface scan was located at the halfway point of the volume scan.

1. Synthesis: Converting PPIs to RHIs

Since the ASR simulator, described in the next section, integrates product data over elevation, it was necessary to convert the PPI (azimuthal scan) volume data to an RHI (elevation scan) format. Each FL-2 PPI volume scan was thus interpolated and resampled to generate synthesized RHIs of DZ, V, and SW. The technique used, a two-dimensional skewed Cressman weighting scheme, is described in Appendix A. The entire azimuthal extent of each volume scan was synthesized; radial range extent was always 10 km, centered upon the event location.

2. Simulation I: Converting RHI Product Data to ASR Time-Series

The ASR-9 simulation program uses a pencil-beam radar's RHI products (DZ, V, and SW) to simulate the time-series output of an ASR radar system. Figure 3 is a block diagram of the data flow through the ASR-9 simulator. Products from each gate are used to generate power spectra. Each of these spectra are weighted by the two-way beam-pattern of the ASR radar, then integrated over elevation. Products from each gate are used to generate power spectra. Each of these spectra are weighted by the two-way beam-pattern of the ASR radar, then integrated over elevation.

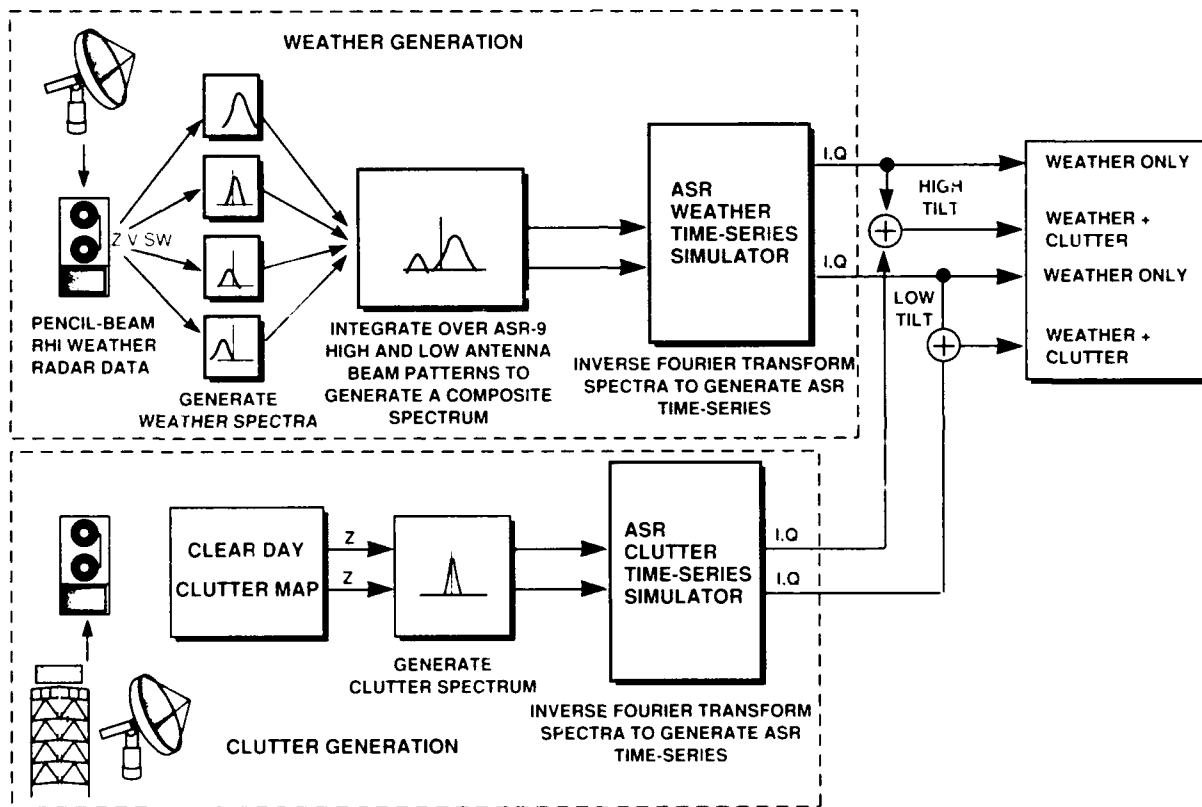


Figure 3. ASR-9 weather and clutter simulation block diagram.

Three noise and randomization components were applied to the spectra:

1. White noise: a constant computed from the FL-3's nominal noise setting was added to the spectra.
2. Statistical variation: The magnitude of each frequency component of the spectra was multiplied by a Rayleigh distributed random variable with a mean of 1.

3. Phase randomization: The phase of each frequency component was uniformly distributed between $-\pi$ and π .

The spectra are then inverse Fourier transformed into 26-pulse time-series, the coherent processing interval currently used by the ASR-9 real-time processor. Data from both high- and low-elevation tilts are simulated.

For this study, most of the radar parameter settings used in the simulation were set to be the same as those of FL-3. Parameters for an ASR-9 are nearly identical, except that pulse length is 1.0 μ s and transmit and receive losses may differ. The maximum range of the R-squared STC function was set to 12.36 km, equivalent to setting the system noise level at 0 dBZ out to 12.36 km. The simulations were run with the nose of the beam at both one and two degrees elevation. Two degrees is the normal operational setting for an ASR. Placing the nose of the beam at one-degree elevation slightly increases an ASR's sensitivity to dry microbursts. However, it also significantly enhances the impact of ground clutter. Operation at one-degree elevation was simulated to examine the effects of this weather/clutter tradeoff.

The block staggered pulse repetition frequency (PRF) of the ASR-9 was not treated in this study due to excessive processing requirements for the simulation. Instead, a constant PRF signal, as used in FL-3 field tests in Huntsville, was simulated. This change does not affect main results of this study.

Table 2 lists the simulator's radar parameter settings. (Note: The antenna elevation was switched to 2.0 degrees for the two-degree simulations.)

C. GENERATING CLUTTER TIME-SERIES FROM PENCIL-BEAM AND FAN-BEAM DATA

This section describes how clutter data collected by FL-2 in Denver and FL-3 in Huntsville were transformed into ASR clutter time-series. This clutter time-series was added to the simulated weather time-series, described above, to simulate ground clutter contamination. The section begins by describing how clear day maps of Denver and Huntsville clutter were generated. Then it describes how these maps were converted to time-series.

1. Clear Day Clutter Map Generation

Both Huntsville and Denver clutter distributions were used. The methods used to generate both sets of maps differed:

Huntsville: Since actual FL-3 fan-beam clutter data from Huntsville were available, these were used to construct a map. Data were selected from 8 September 1988, one of the few days in which clutter data were collected at both one- and two-degree elevations. A single scan (rotation) was used so that the stochastic nature of the clutter echoes was simulated. The all-pass filter "residue" map was then converted to a generic clear day map format. Since the STC function operating in Huntsville set system

Table 2.
ASR Simulated Radar Parameters.

Azimuthal Beamwidth	1.45 degrees
Elevation Beamwidth	6.20 degrees
Transmitted Power	58.7 dBm
Pulsewidth	650 nsec
Antenna Gain - Low Beam	33.5 dB
Antenna Gain - High Beam	32.5 dB
Receiver Gain - High Beam	112.75 dB
Transmitter Loss	-1.5 dB
Receiver Loss - Low Beam	-2.8 dB
Receiver Loss - High Beam	-2.6 dB
Noise - Low Beam	-105.7 dBm
Noise - High Beam	-105.7 dBm
Antenna Elevation [0 dB pt]	1.0 (2.0) degrees
Gate Spacing	0.12 km
Pulse Repetition Frequency	980 Hz
Burst Mode	OFF
Total Pulses	26
Frequency	2730 MHz
STC Range	12.36 km
STC Exponent	2.0

noise for FL-3 to a constant 6.1 dBZ, all values in the clear day map below the equivalent of 6.1 dBZ were thresholded to 0.

Denver: The Denver clear day map was generated from FL-2 pencil-beam data in a series of steps:

1. An FL-2 horizon scan reflectivity (DZ) field, collected on a clear day (13:11:50 26 April 1988) was transformed into a clutter cross-section (σ^0).

2. The σ^0 field was then transformed back to a DZ field, assuming propagation factors corresponding to spherical spreading from the site of the ASR-8 at Stapleton airport.
3. The DZ field was attenuated to account for antenna elevation and beam shape differences between FL-2 and an ASR. Four attenuation factors were computed (for high and low beams at one- and two-degree nose elevations). The factors were computed as follows:

A base attenuation factor was determined to account for beam shape. The median reflectivity observed by the low beam of Stapleton's ASR-8 in 1985 was obtained from a graph in Weber and Moser (1987). This graph is reproduced in Figure 4a. A corresponding graph, computed and plotted from the coordinate-translated FL-2 clutter data prior to attenuation, is shown in Figure 4b. In the heavy clutter regions from 0 to 20 km, the two graphs differed by 14 to 20 dBZ. The base factor was thus set to -17 dB; the two-degree low beam could be reasonably approximated by attenuating the FL-2 Denver clutter data by this base factor.

To approximate clutter for the low beam at one degree and the high beam at one and two degrees, three additional attenuation factors were computed by expressing each beam's clutter illumination power relative to the two-degree low beam (by clutter illumination power it is meant that the amount of power directed at and below the horizon). These relative power values were computed by integrating the two-way ASR beam pattern using measured ASR-9 beam pattern coefficients. All four attenuation factors computed are summarized in Table 3.

4. The attenuation factors were applied to the coordinate-translated Denver clutter maps produced in step 3, and four attenuated clutter fields were generated. These four DZ fields were then transformed into two clear day maps, one map for each antenna elevation. These maps, in reflectivity units, are shown in Figure 5.

2. Simulation II: Clear Day Maps to Clutter Time-Series

The clutter reflectivity data from the two sets of clear day maps were transformed to ASR time-series format by:

1. Generating Gaussian clutter power spectra (spectral width 0.72 m/sec) centered at zero velocity with integrated power proportional to the clutter reflectivity level;
2. Applying Rayleigh amplitude variation and uniform phase randomization, as was done in generating the simulated weather signals. No white noise component was added; and
3. Inverse Fourier transforming the clutter spectra to time-series.

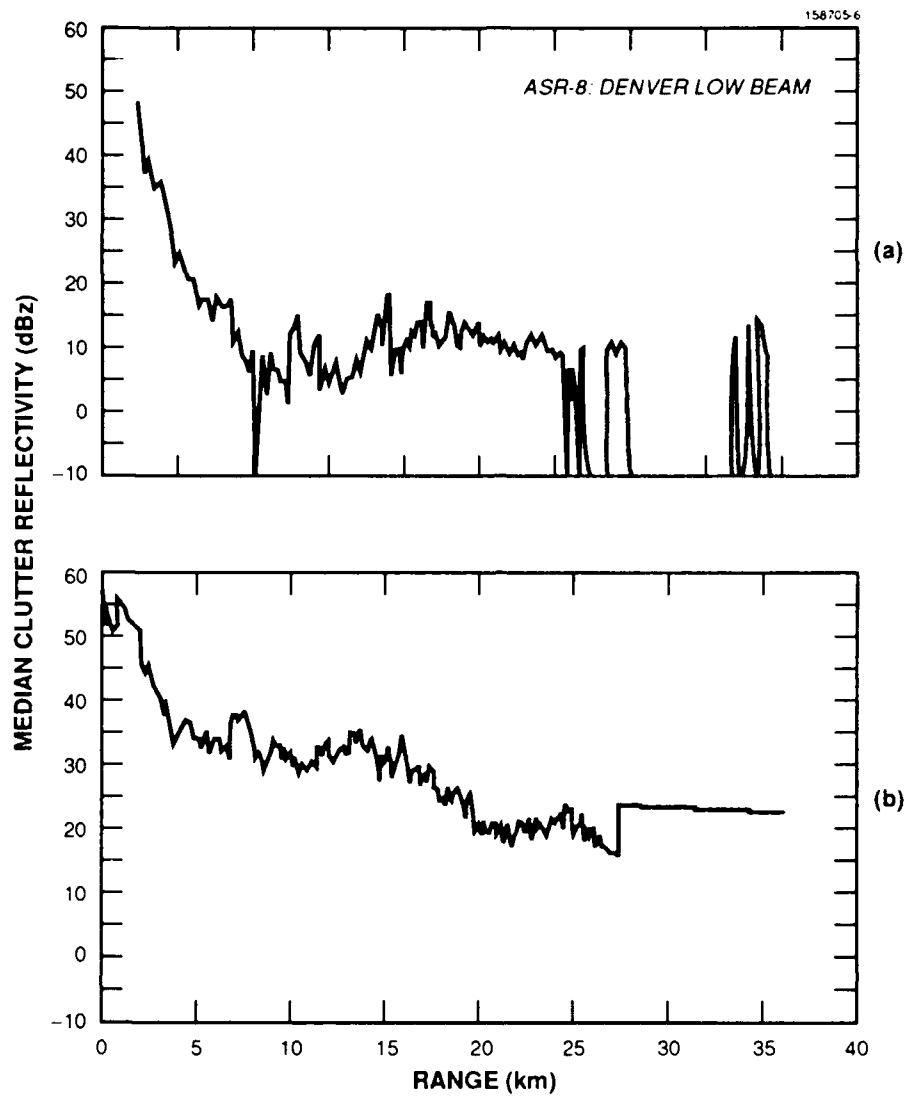


Figure 4. Median ground clutter intensity (ensembled over azimuth) versus range: a) from the ASR-8 at Stapleton Airport (from Weber, 1987); b) from coordinate-translated FL-2 data. These two measured distributions were used to compute the base beam attenuation factor described in the text.

Table 3.
Clear Day Clutter Map
Attenuation Factors

Beam	Antenna Elevation	
	One-Degree	Two-Degree
Low	-10.83 dB	-17 dB
High	-24.49 dB	-32.31 dB

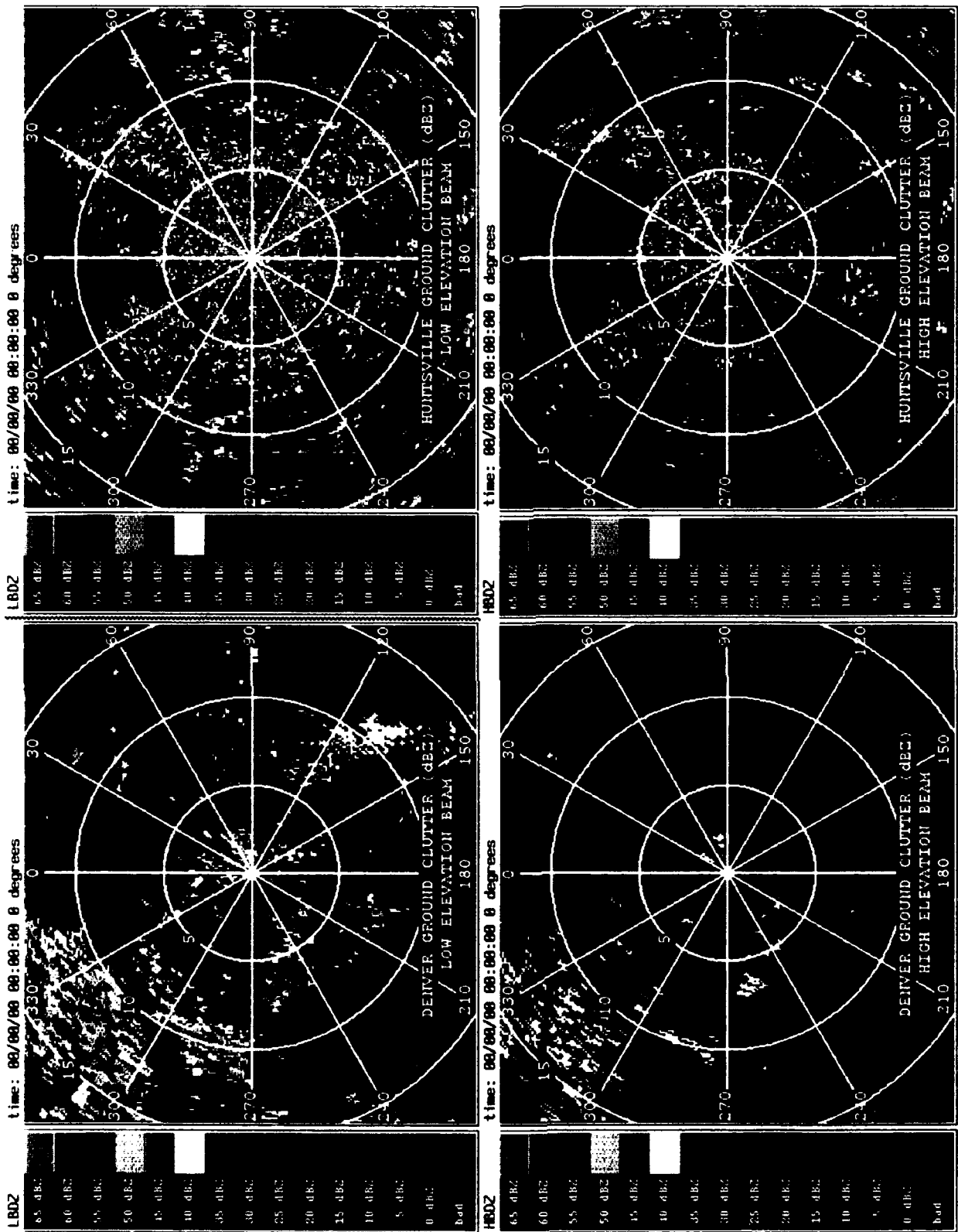


Figure 5. Clutter maps used in dry microburst study, in units of weather reflectivity (dBZ) (range rings at 5 km; azimuth lines every 30 degrees).

As depicted in Figure 3, these clutter time-series were then added to the simulated weather time-series, thus producing clutter contaminated fan-beam ASR time-series weather data from dry microbursts.

D. SIGNAL PROCESSING: GENERATING ASR WEATHER PRODUCTS

All of the simulated time-series were processed using techniques developed for the real-time wind shear detection processor developed for FL-3. All of the simulated weather cases without clutter contamination were processed with no clutter filtering applied. All of the simulated weather with clutter contamination were processed using the appropriate clutter residue map. One of four FIR clutter filters are adaptively selected for each gate of the low beam; the FIR filter selections for the low beam data are also used for high beam data. The generation of the residue maps used is described below.

The ASR signal processor generates several weather products. The two products of importance in this study were:

Low-Beam Velocity (LBV): This Doppler velocity product is computed from the first autocorrelation lag of the low beam data. No high beam information is used.

Dual-Beam Velocity (DBV): This Doppler product is computed using data from both high and low receiving beams of the ASR. The algorithm used in computing this product is described in Weber (1989). In brief, the velocity estimate is computed from a weighted difference of the first autocorrelation lags of the two beams. It has been shown in Weber and Noyes (1988) and in Weber (1989) that the dual beam velocity field is more appropriate for the detection of low altitude wind shear than the low beam product.

The ASR signal processor thresholds out all data with a signal-to-noise ratio less than 7 dB. Since system noise was set via STC to 0 dBZ in the simulated scans, good data with reflectivity below 7 dBZ would be thresholded out. The signal processor also thresholds all data where the signal-to-clutter ratio is less than 10.4 dB. Since a goal of this study was to determine whether the events were detectable at all, regardless of false alarms, all of the cases were processed both with the default settings and with signal-to-noise thresholding switched off and signal-to-clutter thresholding lowered to 5 dB.

1. Clutter Residue Map Generation

All clutter residue maps, used for adaptive filter selection in the ASR signal processor, were generated using the same data and methods described in section C for generating the clear day maps. All four filter outputs of the ASR signal processor contributed to the residue map rather than the all-pass filter output alone. The only other differences in generating them were:

Huntsville: Rather than using a single scan of FL-3 data, three scans were averaged after being processed.

Denver: To simulate the effects of scan averaging, the exponential statistical variation functions in the program used to generate the simulated Denver clutter time-series were disabled. To remain consistent with the sensitivity limit of the FL-3 data from Huntsville, the 6.1 dBZ threshold was applied to this map as well.

E. MICROBURST DETECTION ALGORITHM

The microburst detection algorithm used, described in Weber and Noyes (1988), is a slightly modified version of the microburst divergent outflow detection algorithm (MDOA) developed for the TDWR. Briefly, the process used to generate microburst alarms is as follows:

1. Shear Segments: The algorithm searches for shear segments, runs of velocities increasing with range. Steps are taken to deal with spurious jumps in velocity or small data gaps.
2. Clusters: Range overlapping segments are azimuthally associated into shear segment clusters, thus defining a shear region.
3. Microburst Alarms: Relying upon the ASR's 4.8 sec update rate, shear regions are time-associated into microburst alarms on successive scans of the radar. In this way, many spurious shear regions are rejected.

The FL-2 Denver scanning strategy provided surface scan coverage only once a minute. As a result, generation of multiple simulated scans for time-association was not possible. This study, therefore, uses only shear clusters, the product of step 2, in its assessment of an ASR's microburst detection capability. This eliminates an important false alarm filter but does not lower detection performance since clusters must first be generated before producing microburst alarms.

3. RESULTS

A. CASE STUDIES

This section discusses the analysis of four of the 11 simulated dry microbursts. The first case described was a very dry event which was detectable in the absence of clutter, but obscured when clutter was added. The second was a dry event detectable under virtually all conditions. The third and fourth, which occurred within 70 minutes of each other, were marginally detectable events; the meteorological environment in which they occurred also was conducive to numerous false alarms.

1. Case 08 - 08 August 1988, 20:41 GMT

On August 8, 1988 a very dry microburst occurred 6 km from the FL-2 radar site in Denver. A near surface radial shear of 22 m/sec was measured by the FL-2 pencil-beam radar at the time of maximum shear (20:41 GMT). Near surface reflectivity for this event was extremely low (5 dBZ). Like many low reflectivity microbursts, this event descended from the anvil structure of a higher reflectivity convective storm, located approximately 10 km west of the radar. Figures 6a-d show reflectivity and radial velocity fields from two of the 15 PPI scans from which the three-dimensional storm profile used in the simulation was constructed. The microburst event is centered at 316 degrees azimuth in the radial velocity field of the 0.3-degree elevation scan, Figure 6b. In the 30.1-degree elevation horizontal scan, Figure 6c, the anvil from the storm at 255 degrees clearly extends over the area of the microburst event. Figure 7 shows an interpolated vertical cross-section of the event, constructed from the 15 PPI scans. The cross-section reveals both anvil cloud and the precipitation accompanying the downdraft. Note the decrease in reflectivity as this precipitation approaches the surface, indicative of the evaporation of the hydrometeors.

As described in Section 2.B, the interpolated three-dimensional data were fed into the ASR-9 simulator. Figure 8 shows velocity fields generated from processing the resultant simulated time-series signal with the Lincoln Laboratory ASR signal processor. Note at this stage that no clutter signals have been added. Low-beam reflectivity (LBDZ), low beam velocity (LBV), and dual beam velocity (DBV) are shown. In the both the LBV and DBV fields, shear segments and associated regions are represented by red lines and red boxes, respectively. The microburst was readily detectable in the DBV field, Figure 8c. The microburst detection algorithm successfully associated the shear segments azimuthally, generated shear regions, and estimated a differential velocity of 17.8 m/sec. In regions outside of the event, inbound (negative velocity) overhanging precipitation was mapped into the ASR velocity field, particularly beyond 9 km in range in regions due west of the radar. This is evident in both LBV and DBV fields.

Figure 9 shows the effect of adding Denver and Huntsville clutter time-series to the simulated weather data time-series and applying appropriate filtering operations in signal processing. In the neighborhood of the microburst, the effective reflectivity of the ground clutter, prior to clutter filtering, was 7 dBZ for Denver, 33 dBZ for Huntsville. Not surprisingly, the event was completely swamped by ground clutter residue in the Huntsville clutter environment. In the Denver case, where the clutter was of a comparable level to the weather reflectivity, the event was detected in the low beam velocity field (figure 9b) and only marginally missed in the dual beam field (Figure 9d). Note again that the normal signal-to-noise and signal-to-clutter thresholds have been removed, resulting in high variance for the velocity estimates in regions of low signal strength.

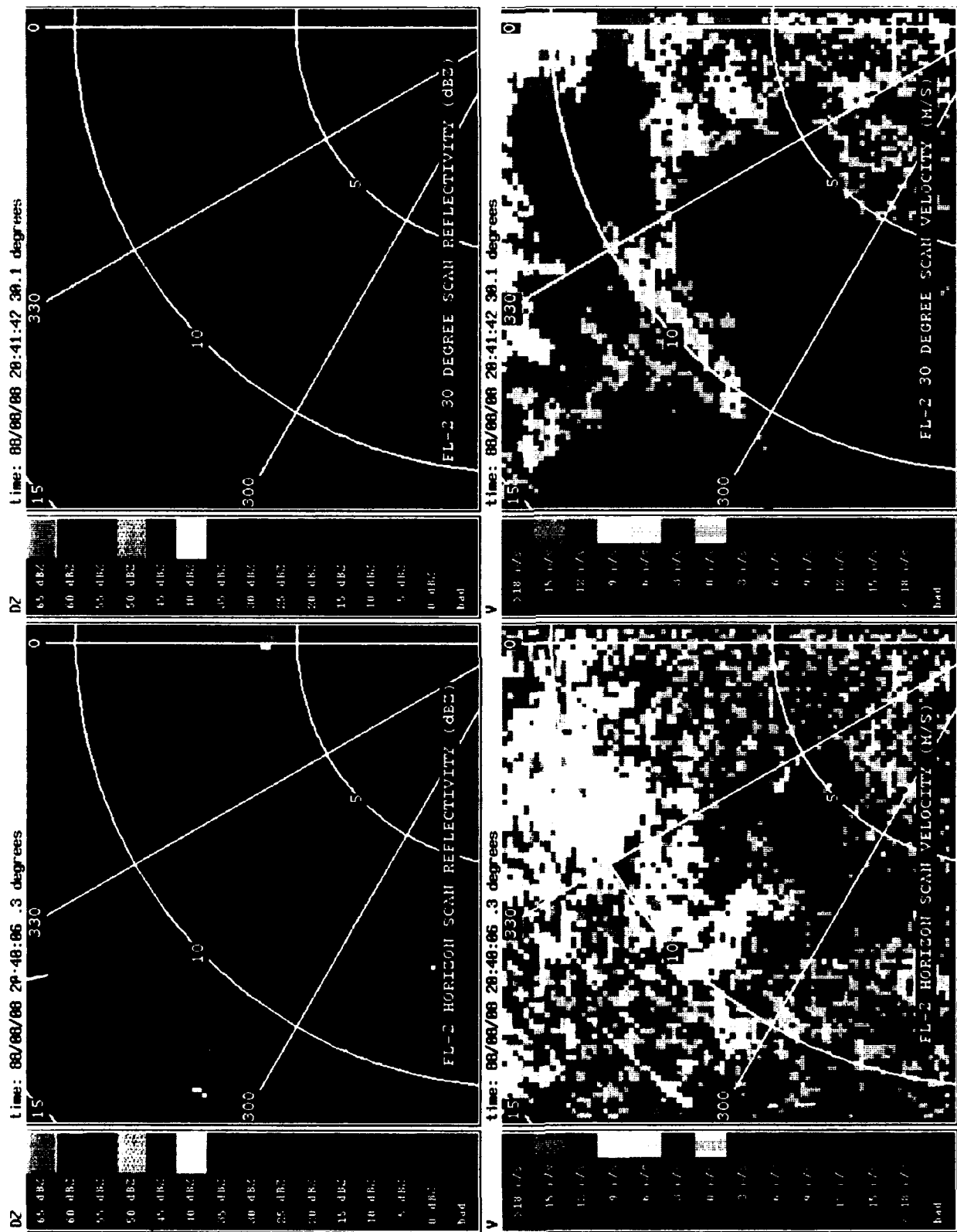


Figure 6. FL-2 pencil-beam reflectivity and radial velocity fields during 5 dBZ dry microburst at 8 km, 316 degrees azimuth, at 20:41 (GMT), August 8, 1988 in Denver. Shown are horizontal scans from 0.3 and 30.0 degrees elevation. (Range rings are at 5 and 10 km; azimuth lines every 30 degrees.)

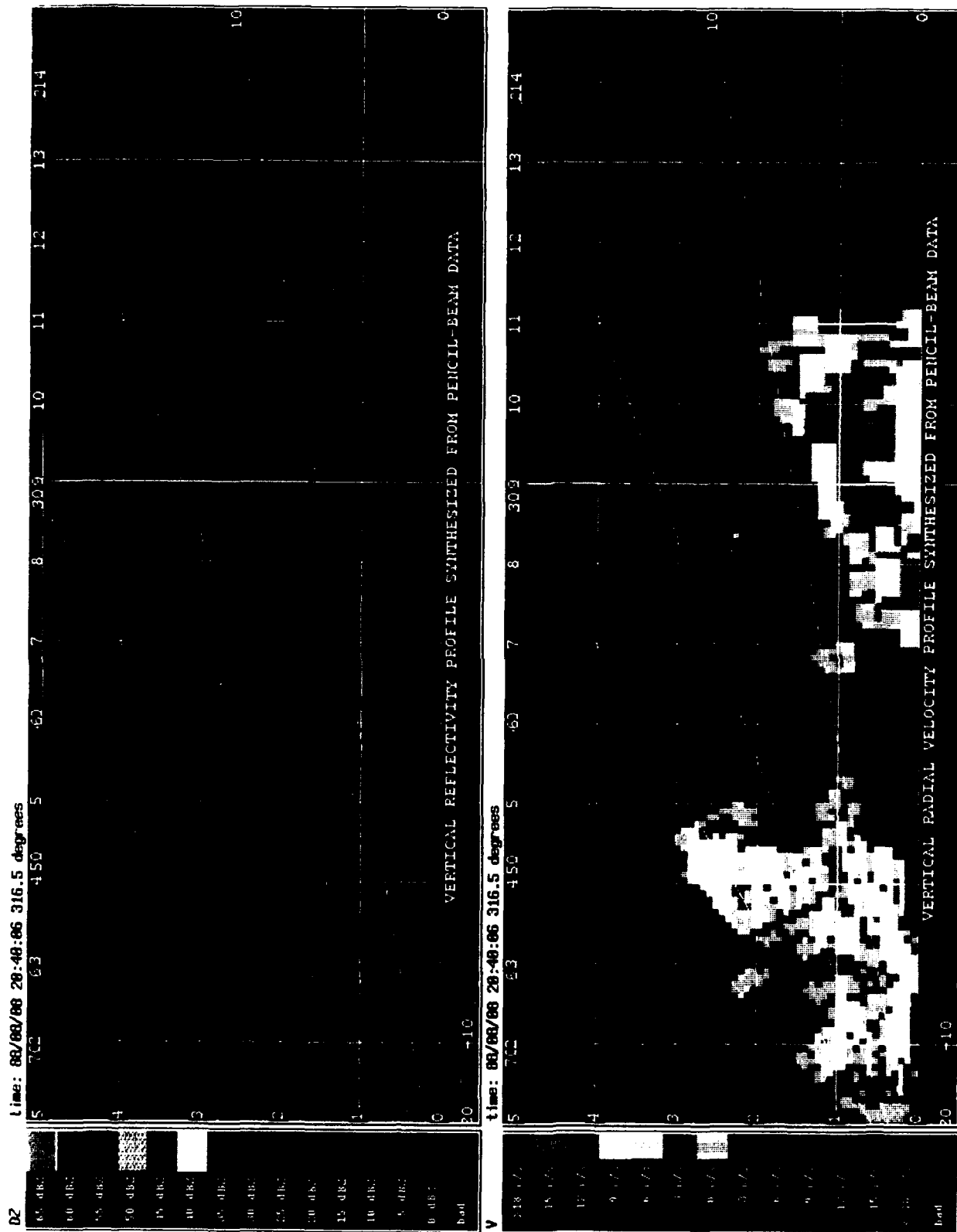


Figure 7. Vertical profile of 20:41 (GMT), August 8, 1988 dry microburst event. Profile was synthesized from 15 horizontal scans taken by FL-2 (ordinate and abscissa scales in kilometers).

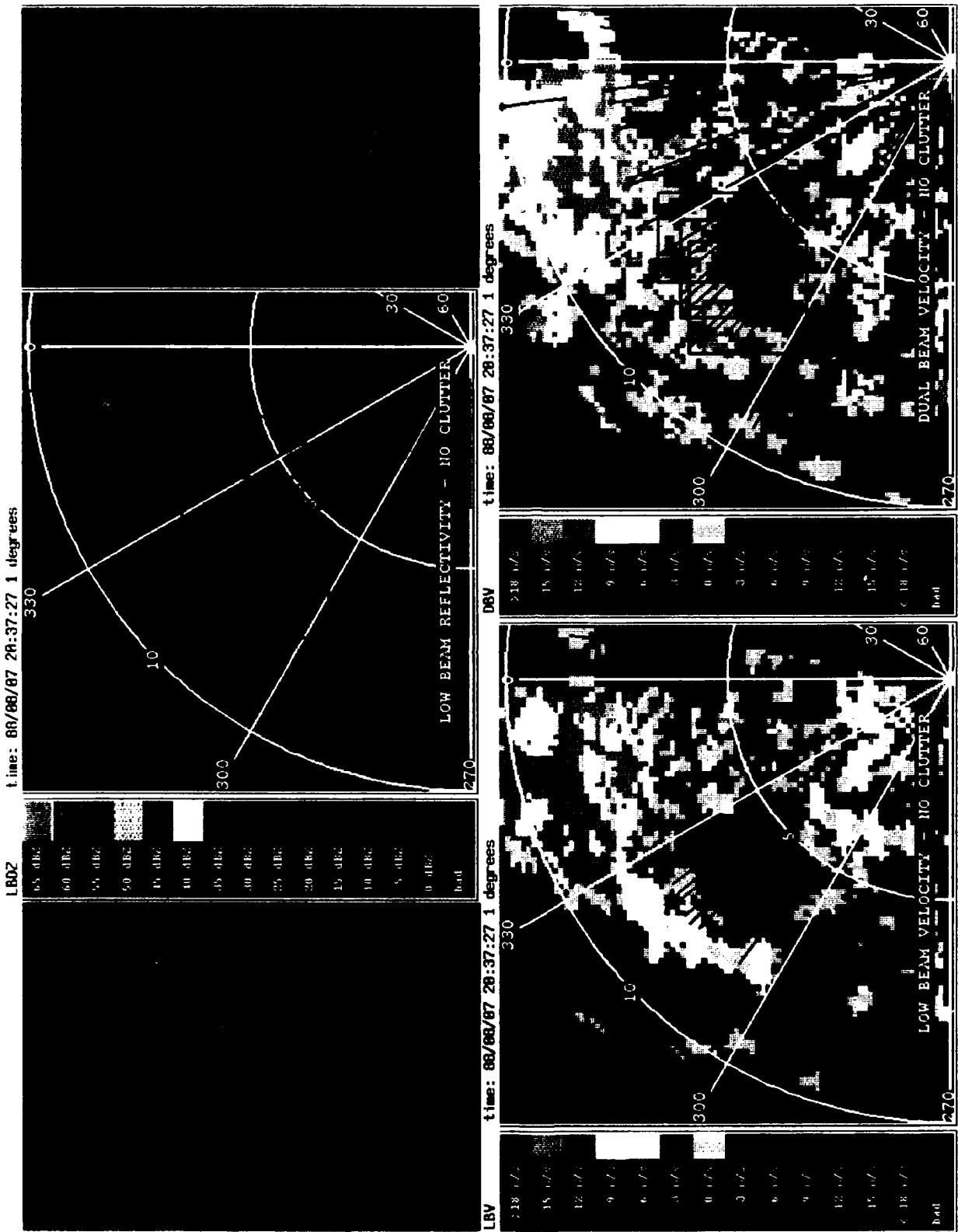


Figure 8. Simulated ASR reflectivity and velocity fields for 20:41 (GMT), August 8, 1988 dry microburst event. No clutter signals have been added. Shear segments and associated regions are represented by red lines and red boxes, respectively (range rings at 5 km; azimuth lines every 30 degrees).

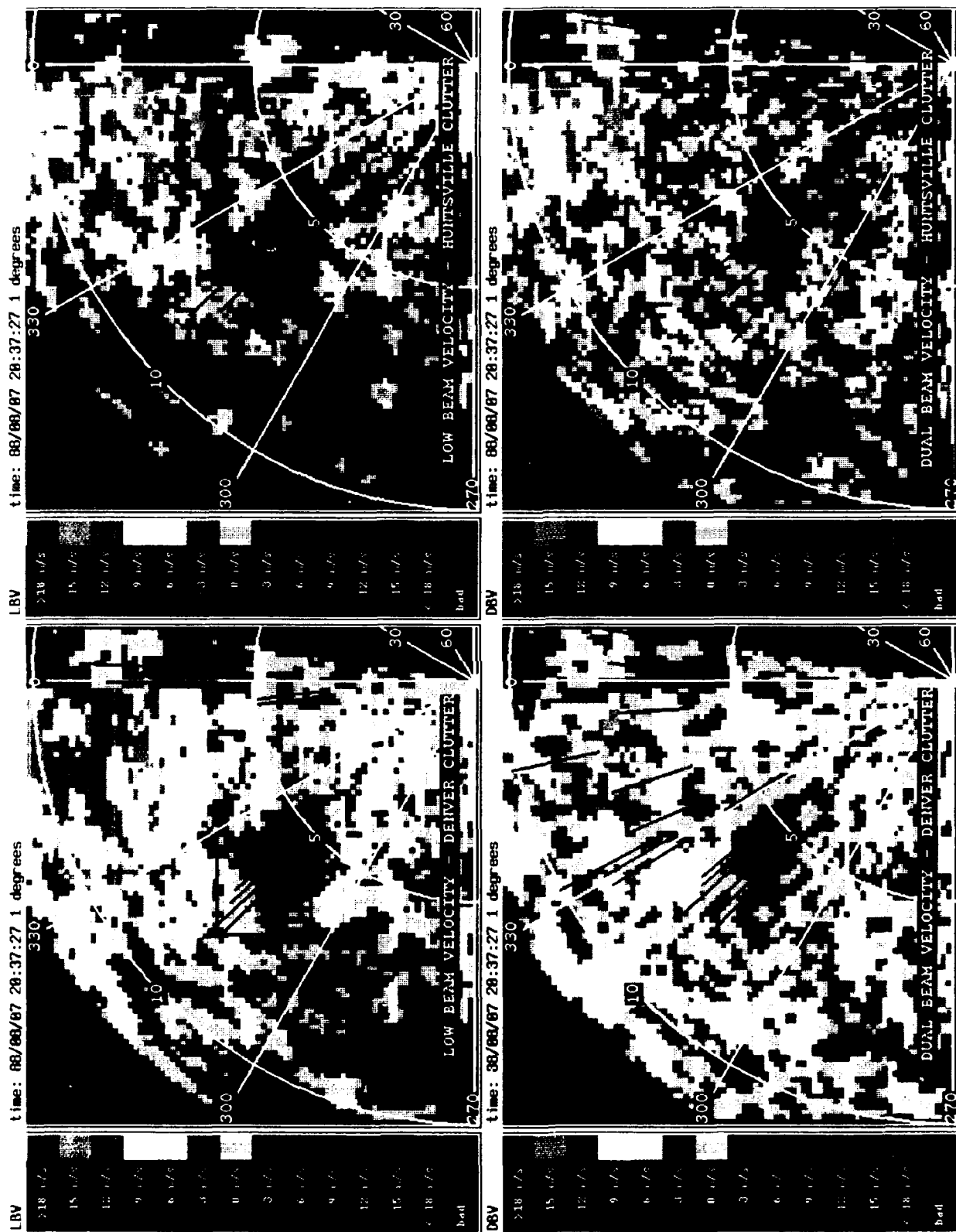


Figure 9. Simulated clutter-contaminated ASR velocity fields for 20:41 (GMT), August 8, 1988 dry microburst event. Shear segments and associated regions are represented by red lines and red boxes, respectively (range rings at 5 km; azimuth lines every 30 degrees).

2. Case 01 - 12 June 1987, 23:07 GMT

On June 12, 1987 a very strong, deep, dry microburst occurred 6 km southwest of the radar in Denver. A near surface radial velocity differential of 24 m/sec was measured by the FL-2 pencil-beam radar at the time of maximum intensity. The FL-2 pencil-beam 0.2-degree elevation scan is shown in Figure 10. In addition to the event of interest, another wind shear event is present in the figure, centered at 13 km range and 285 degrees azimuth. The peak surface reflectivity of this event was 25 dBZ, disqualifying it from this particular study. The high reflectivity returns in regions within 5 km of the radar and in the narrow band centered at 7.5 km west of the radar are ground clutter residue from the FL-2 radar. While this clutter residue does impinge with the outward (positive) velocity component of the wind shear signature of interest, the clutter interference begins beyond the peak velocity, so this slight data corruption should not change the major results of this simulation.

Figure 11 shows the vertical cross-section synthesized from the 14 PPI scans used. The depth of the microburst event is readily apparent from the velocity field (Figure 11b); the outflow region extends almost a half kilometer above the surface.

Figure 12 shows the velocity fields from the processed simulated two-degree elevation fan-beam data. The depth of the outflow and its 20 dBZ surface reflectivity enabled it to be readily detectable. The DBV product for the pure weather case is shown in Figure 12a. Several associated clusters were found in the microburst region. Presumably, in an operational system, these clusters would themselves be associated to generate a single microburst alarm for that event. DBV products subsequent to adding the Denver and Huntsville clutter time-series are shown in Figures 12b and 12c, respectively. The microburst signature was found by the algorithm in the DBV product in both regimes. In the neighborhood of the microburst, the effective reflectivity of the unfiltered ground clutter was 4 dBZ for Denver and 32 dBZ for Huntsville.

3. Case 06 - 10 June 1988, 22:13 GMT

On the afternoon of June 10, 1988, several large storms passed from west to east, just south of the FL-2 radar. Anvils from these storms produced two of the microbursts used in this study. At the time of the first microburst event, 22:10 GMT, a very large, mature, severe thunderstorm was just south of the radar. Figure 13a and b show the 0.3-degree FL-2 surface scan. The microburst event was centered 13 km from the radar at 265 degrees azimuth. Peak near surface radial velocity differential, as measured by the pencil-beam radar system, was 27 m/sec. Peak surface reflectivity in the outflow was 10 dBZ. In the 21.8-degree horizontal scan, Figures 13c and d, part of the anvil structure aloft contributing to the microburst is apparent. The anvil is not directly associated with the higher reflectivity convection at 5 km. Were this the case, then the hydrometeors in the anvil would exhibit a radial velocity away from the cell. Figure 14, a vertical cross-section synthesized from 14 PPI scans, shows that the radial velocity of the precipitation aloft is clearly moving toward the nearer storm. The reflectivity aloft contributing to the microburst is from the larger, severe thunderstorm storm 7 km south of the microburst, beyond the FL-2's scan region.

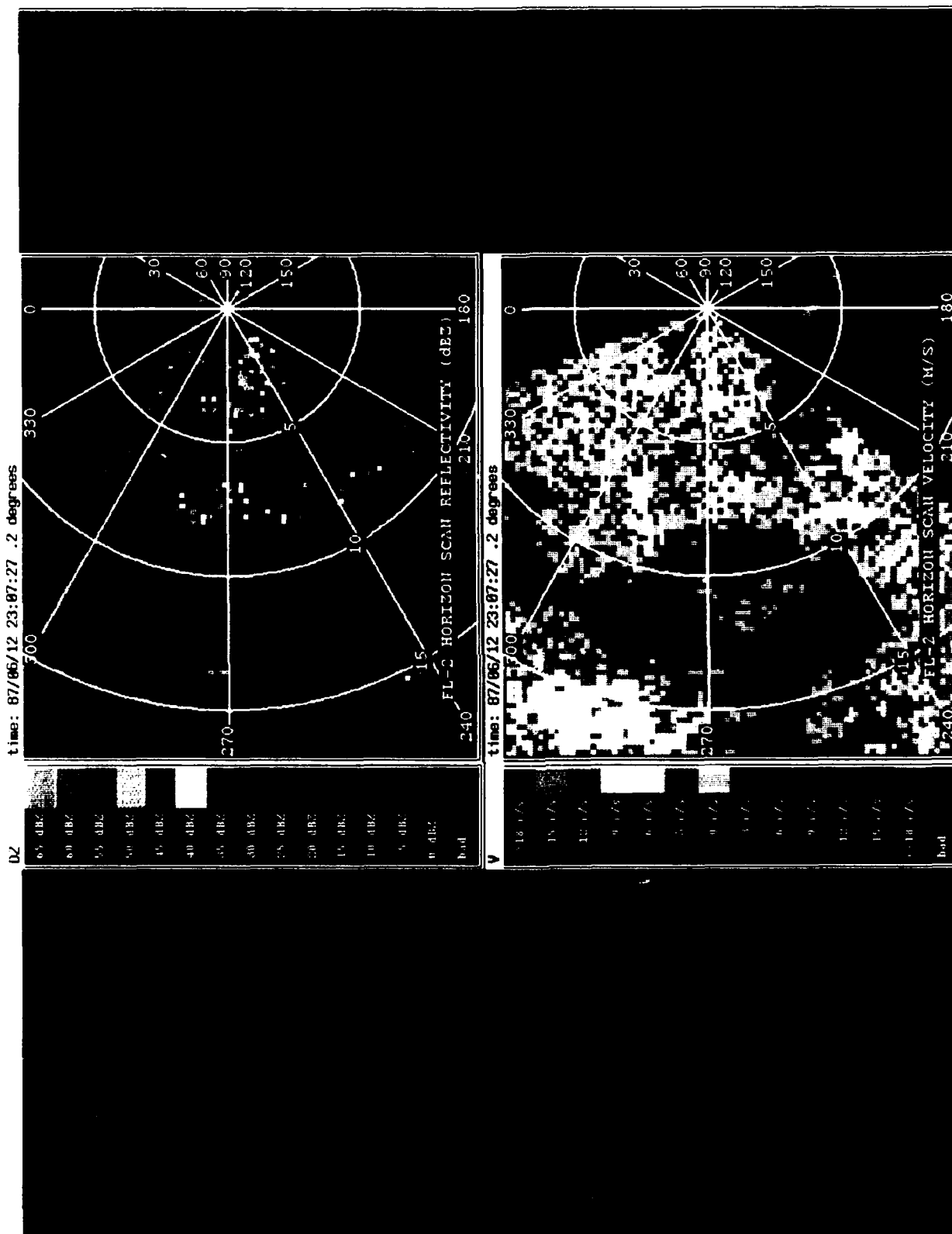


Figure 10. FL-2 pencil-beam reflectivity and radial velocity fields during 15 dBZ dry microburst at 6 km, 219 degrees azimuth at 23:07 (GMT), June 12, 1987 in Denver. Shown is horizontal scan from 0.2 elevation (range rings at 5 km; azimuth lines every 30 degrees).

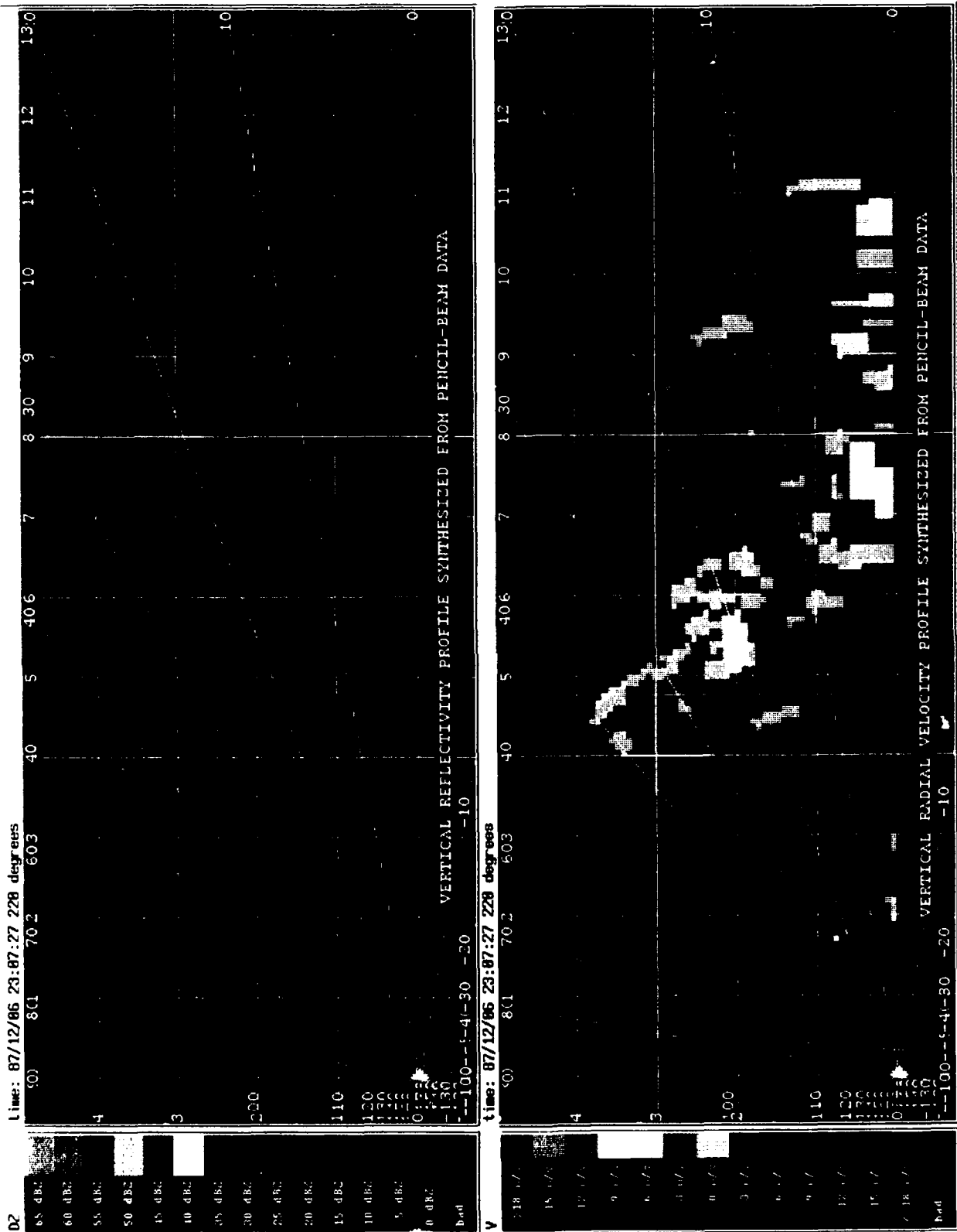


Figure 11. Vertical profile of 23:07 (GMT), June 12, 1987 dry microburst event. Profile was synthesized from 14 horizontal scans taken by FL-2 (ordinate and abscissa scales in kilometers).

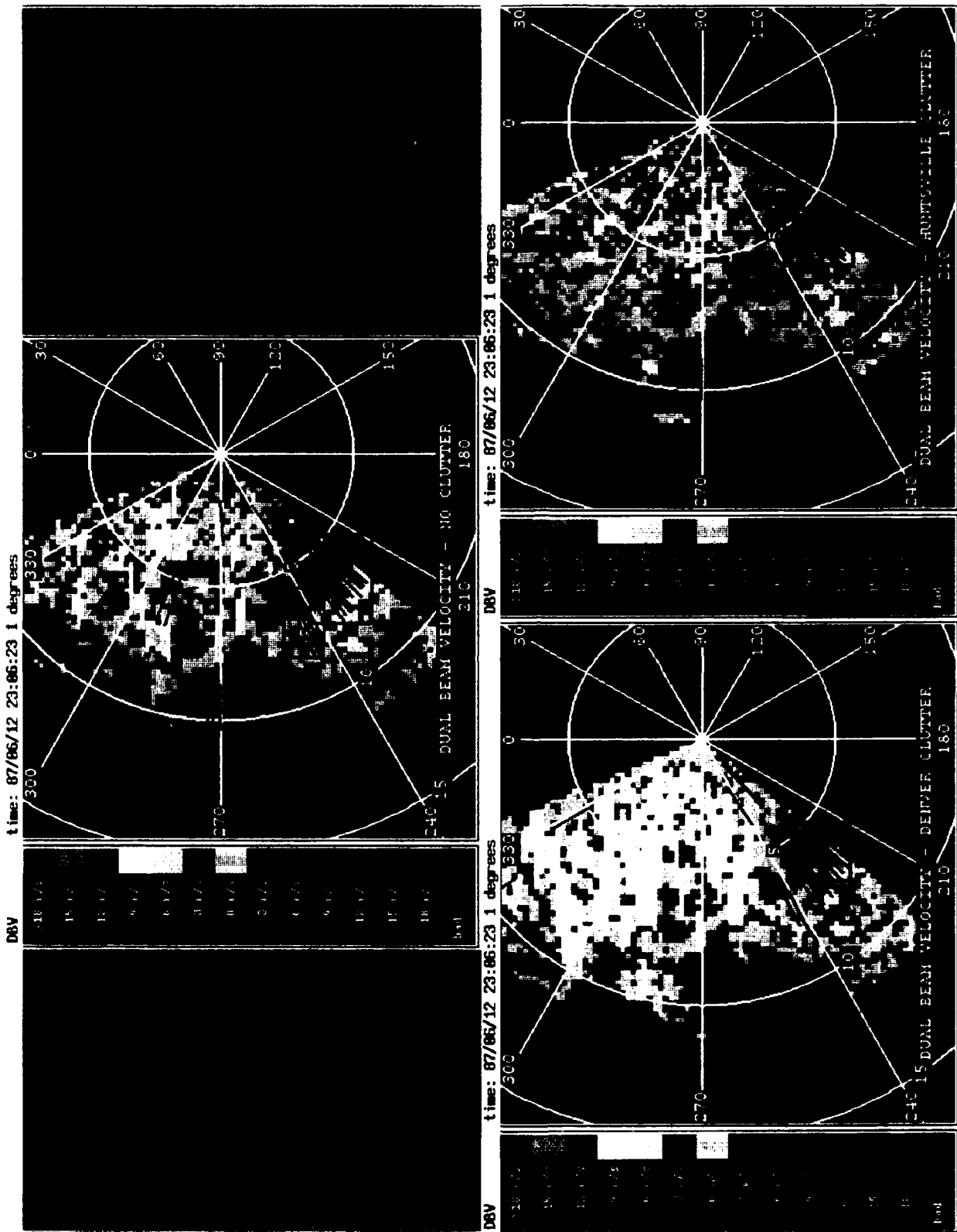


Figure 12. Simulated ASR velocity fields for 23:07 (GMT) June 12, 1987 dry microburst event. Simulations with no clutter, Denver clutter, and Huntsville clutter are shown. Shear segments and associated regions are represented by red lines and red boxes, respectively (range rings at 5 km; azimuth lines every 30 degrees).

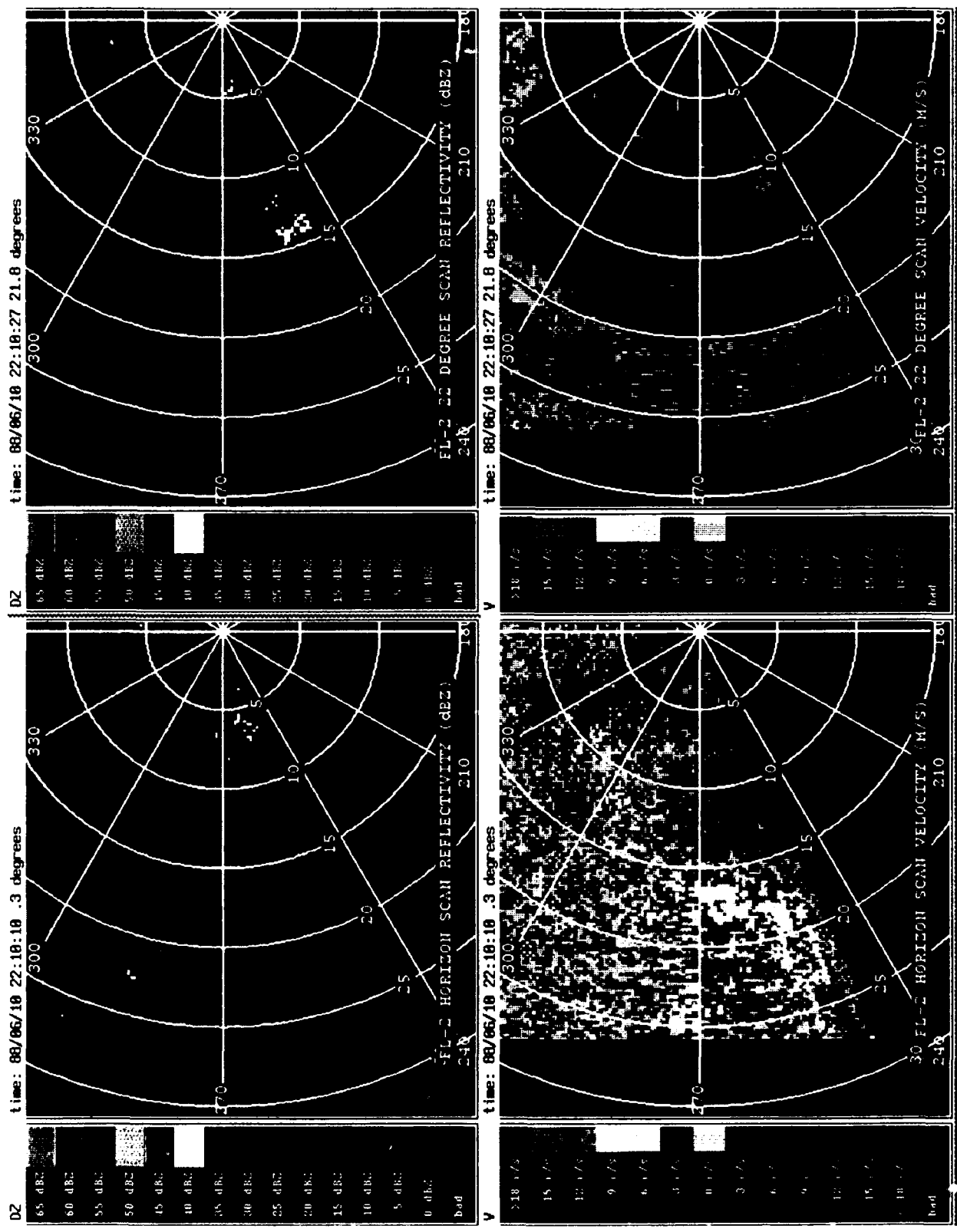


Figure 13. FL-2 pencil-beam reflectivity and radial velocity fields during 10 dBZ dry microburst at 13 km, 265 degrees azimuth at 22:10 (GMT), June 10, 1988 in Denver. Shown are horizontal scans from 0.3 and 21.8 degrees elevation (range rings at 5 km; azimuth lines every 30 degrees).

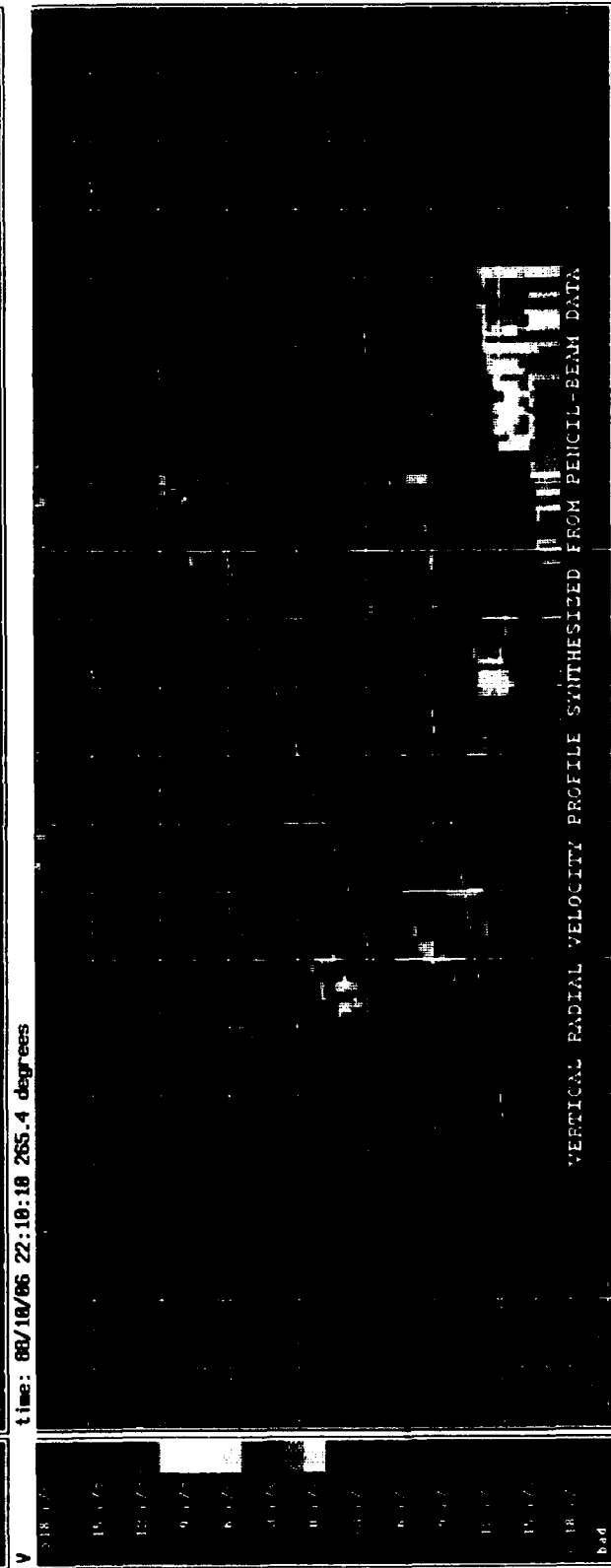


Figure 14. Vertical profile of 22:10 (GMT) June 10, 1988 dry microburst event. Profile was synthesized from 14 horizontal scans taken by FL-2 (ordinate and abscissa scales in kilometers).

Figure 15 shows the DBV products of the two-degree elevation simulated data after signal processing and application of the microburst detection algorithm. In the pure weather case (Figure 15a, the microburst signature was found, along with four false associations. In the clutter contamination experiments, the effective reflectivity of the ground clutter in the neighborhood of the microburst was 25 dBZ for Denver and 16 dBZ for Huntsville. Figures 15b and c show the resultant ASR products from both clutter cases. In both, a divergent outflow signature is visually apparent and the algorithm correctly identified the microbursts in all three cases. However, a single false association occurs in each of these two clutter cases as well.

Applying the default thresholds did not eliminate all of the false associations. Figure 16 shows the resultant images when this case was re-processed using default signal-to-noise and signal-to-clutter thresholding. The "no clutter" case (Figure 16a) had three false associations, while the Denver case had one. The Huntsville false association, however, was eliminated.

4. Case 07 - 10 June 1988, 23:19 GMT

This dry microburst occurred 70 minutes after the event described above, at 12 km and 256 degrees azimuth, 2 km northwest of the location of its predecessor. The very large storm which had produced the first event had by this time moved 20 km to the east, and a new storm developing to the southwest of the radar produced the anvil from which the dry microburst descended. Figure 17 shows the 0.3-degree scan and the 18.6-degree scan from the FL-2 pencil beam radar. Figure 18 shows the vertical cross-section of the event constructed from 14 PPI scans from FL-2.

Figure 19 shows the DBV products of the two-degree elevation simulated data after signal processing and application of the microburst detection algorithm. In the "no clutter" case (Figure 19a), the microburst signature was found. Note that in this case, the marked increase in reflectivity above 1 km altitude (the level at which the radial wind component reversed sign) resulted in widespread mapping of the negative velocities aloft into the ASR velocity field. "Detection" of the microburst signature must be considered fortuitous given that the ASR velocity estimates would not have adequately represented the overall flow field.

In the clutter contamination experiments, the effective reflectivity of the ground clutter in the neighborhood of the microburst was 18 dBZ for Denver and 27 dBZ for Huntsville. Figures 19b and 19c show the resultant ASR products from both clutter cases. In both, a divergent outflow signature is visually apparent; the algorithm failed in the Huntsville case, however, because ground clutter residue fragmented too many shear segments. As in the previous case study, the "no clutter" case had four false associations occurring in regions outside the event. No false associations occurred in the Denver case, but one occurred in the Huntsville case.

Figure 20 shows the same cases after applying the default signal-to-noise and signal-to-clutter thresholds (7 dB and 10.4 dB, respectively). In the "no clutter" and the Denver clutter case, the default thresholds eliminated all detections, valid and false. In the Huntsville case, the false alarms disappeared. Moreover, the algorithm made a valid association where it had failed previously. The new detection occurred because the 10.4 dB signal-to-clutter thresholding enabled heavier clutter filters to be selected in the region of the microburst. The larger stopband widths in these filters biased upward the radial velocity estimates in the event region sufficiently so that the microburst detection algorithm's criteria were met.

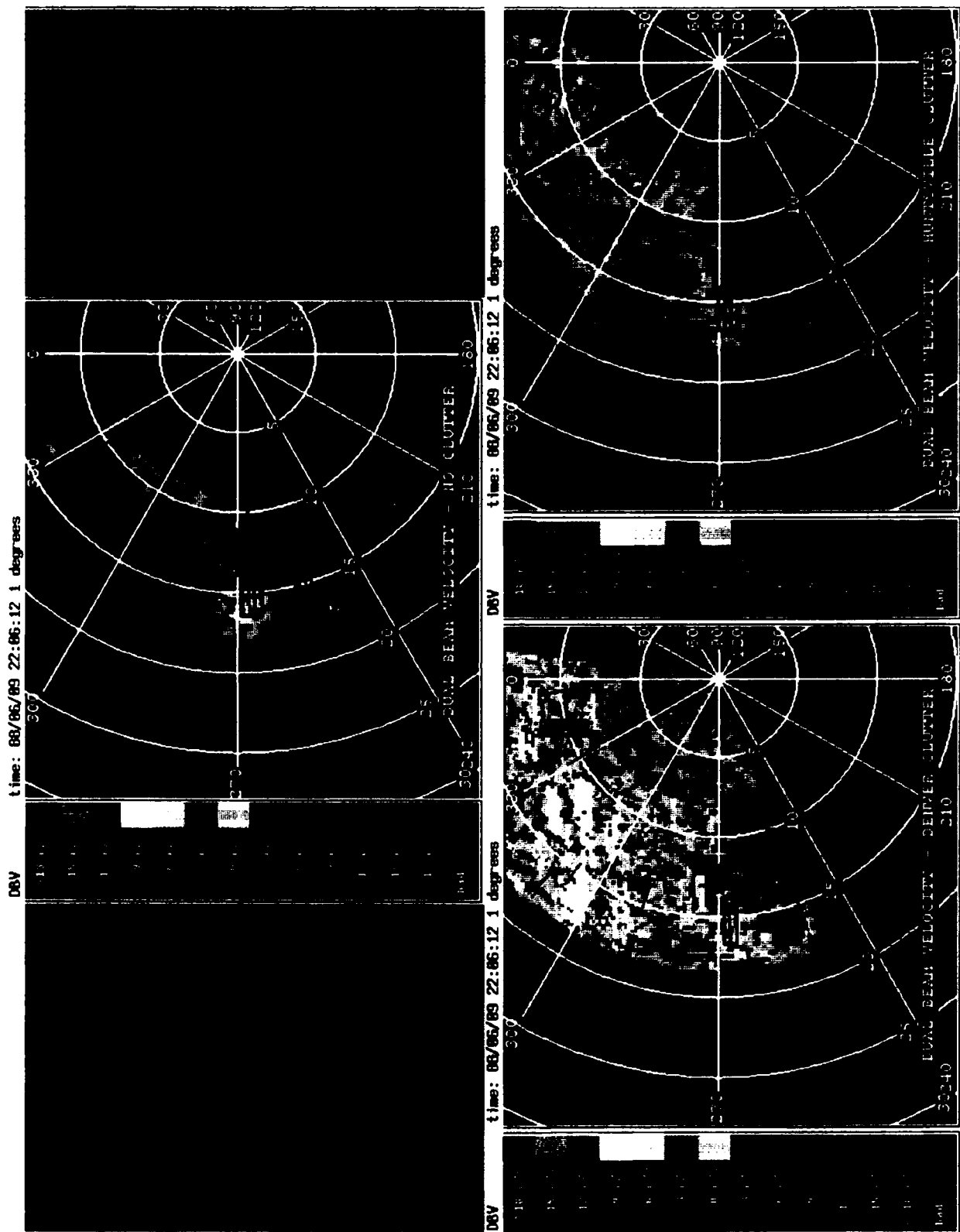


Figure 16. Simulated ASR velocity fields for 22:10 (GMT) June 10, 1988 dry microburst event. Simulations with no clutter, Denver clutter, and Huntsville clutter are shown. Signal-to-noise and signal-to-clutter thresholds are set to default levels. Shear segments and associated regions are represented by red lines and red boxes, respectively (range rings at 5 km, azimuth lines every 30 degrees).

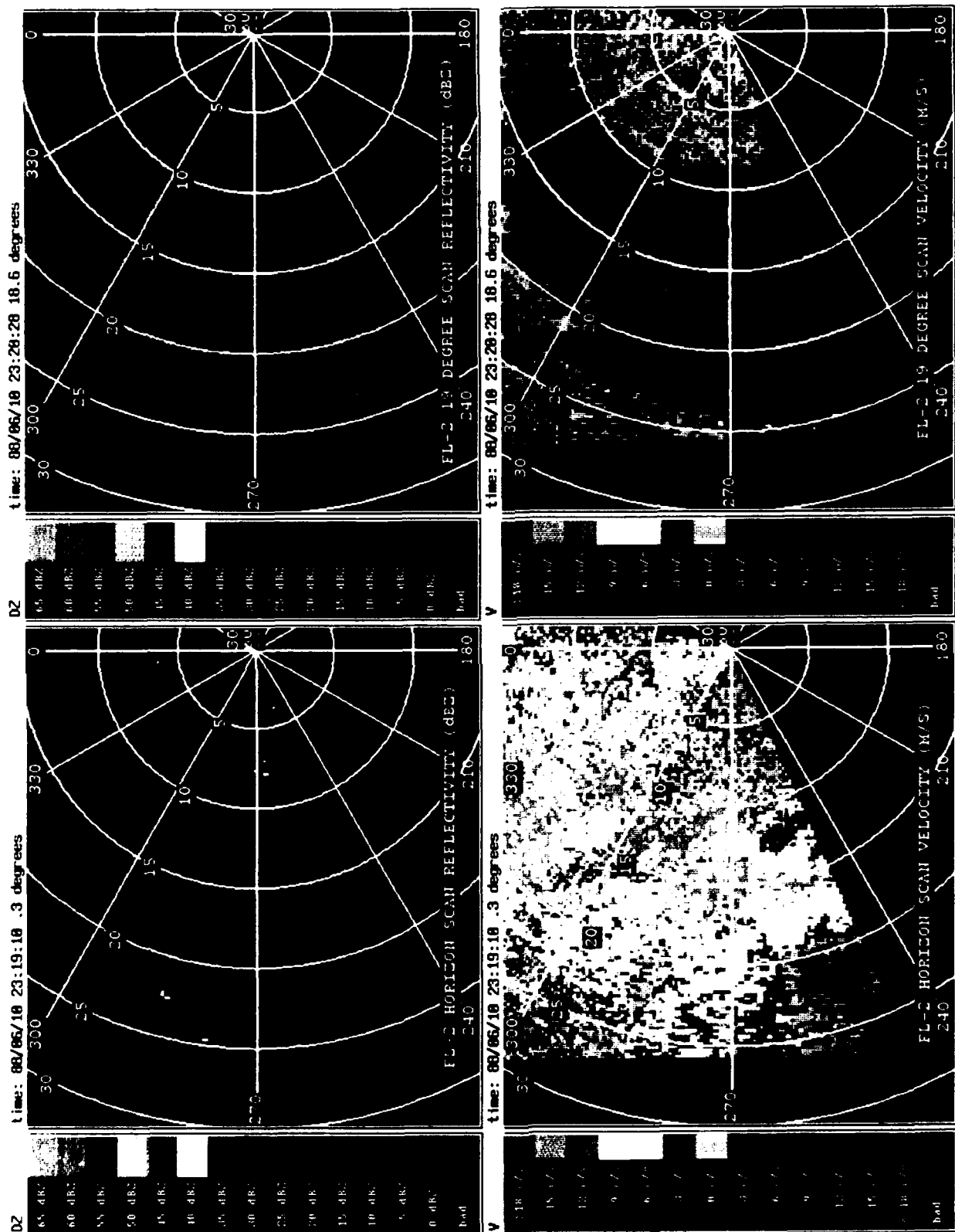


Figure 17. FL-2 pencil-beam reflectivity and radial velocity scans from 0.3 and 18.6 degrees elevation (range rings at 5 km; azimuth lines every 30 degrees).

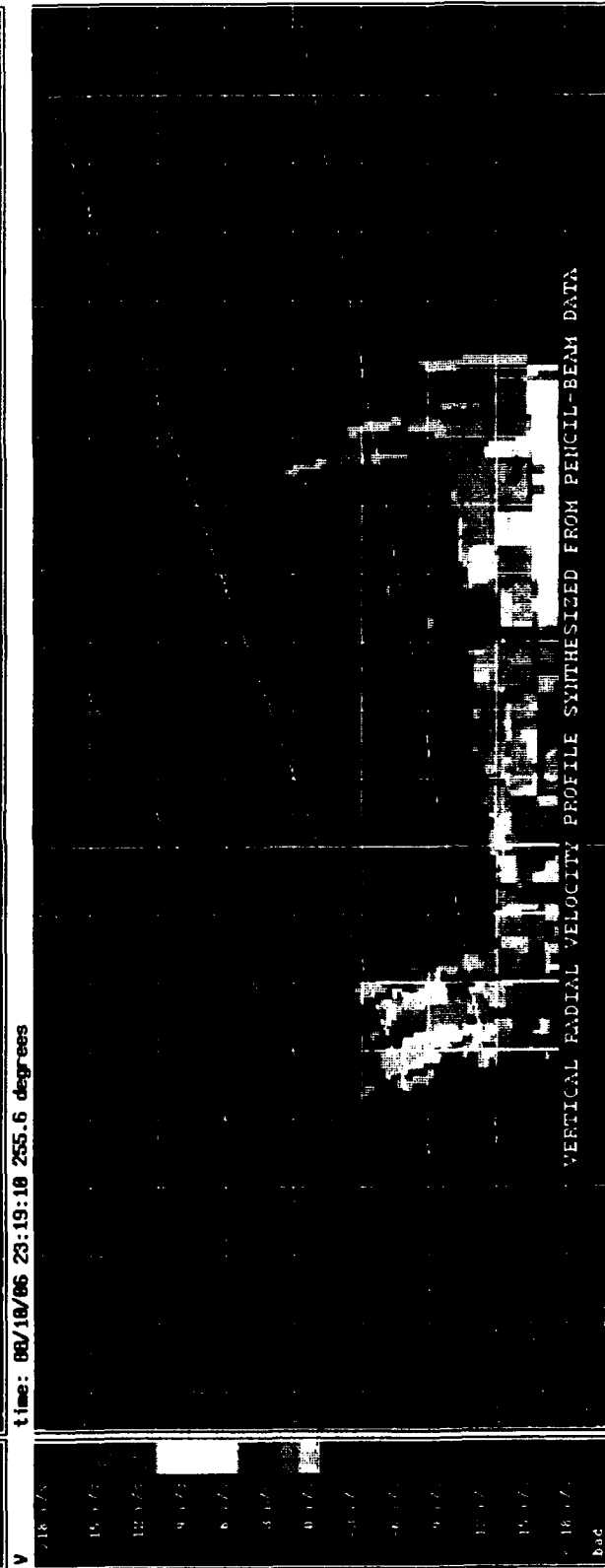
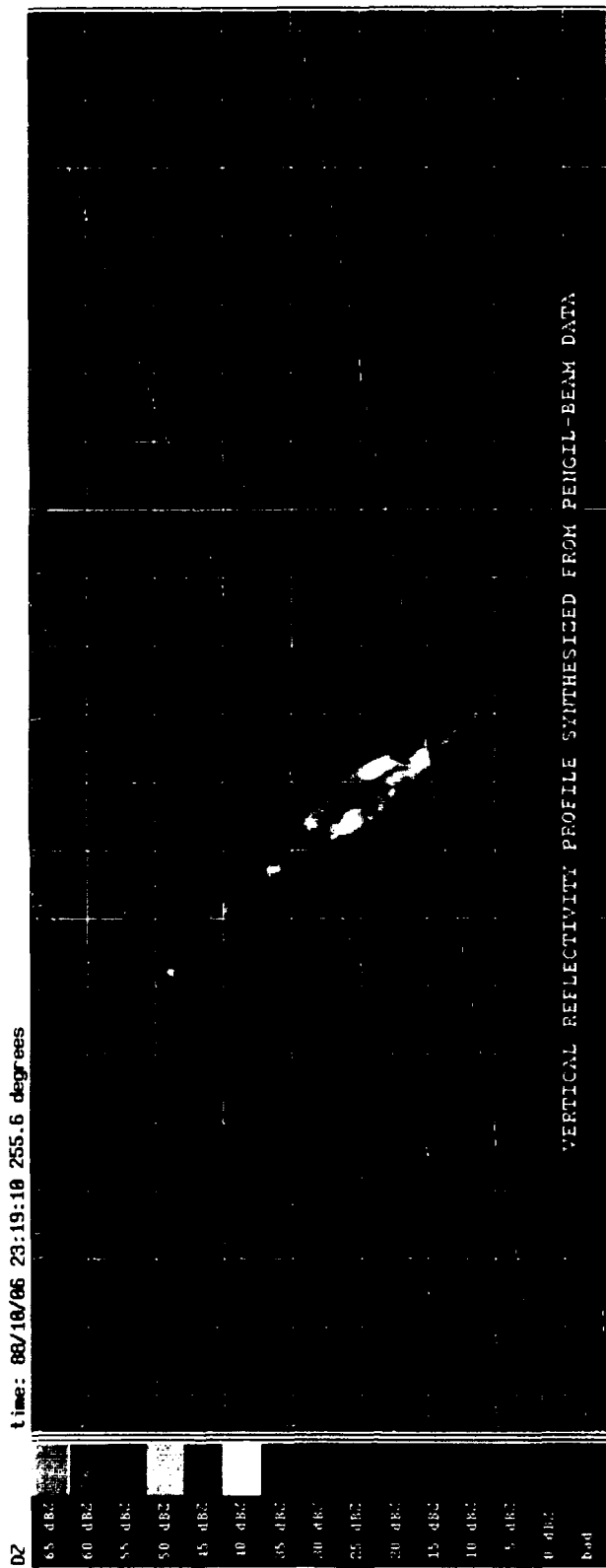


Figure 18. Vertical profile of 23:19 (GMT) June 10, 1988 dry microburst event. Profile was synthesized from 14 horizontal scans taken by FL-2 (ordinate and abscissa scales in kilometers).

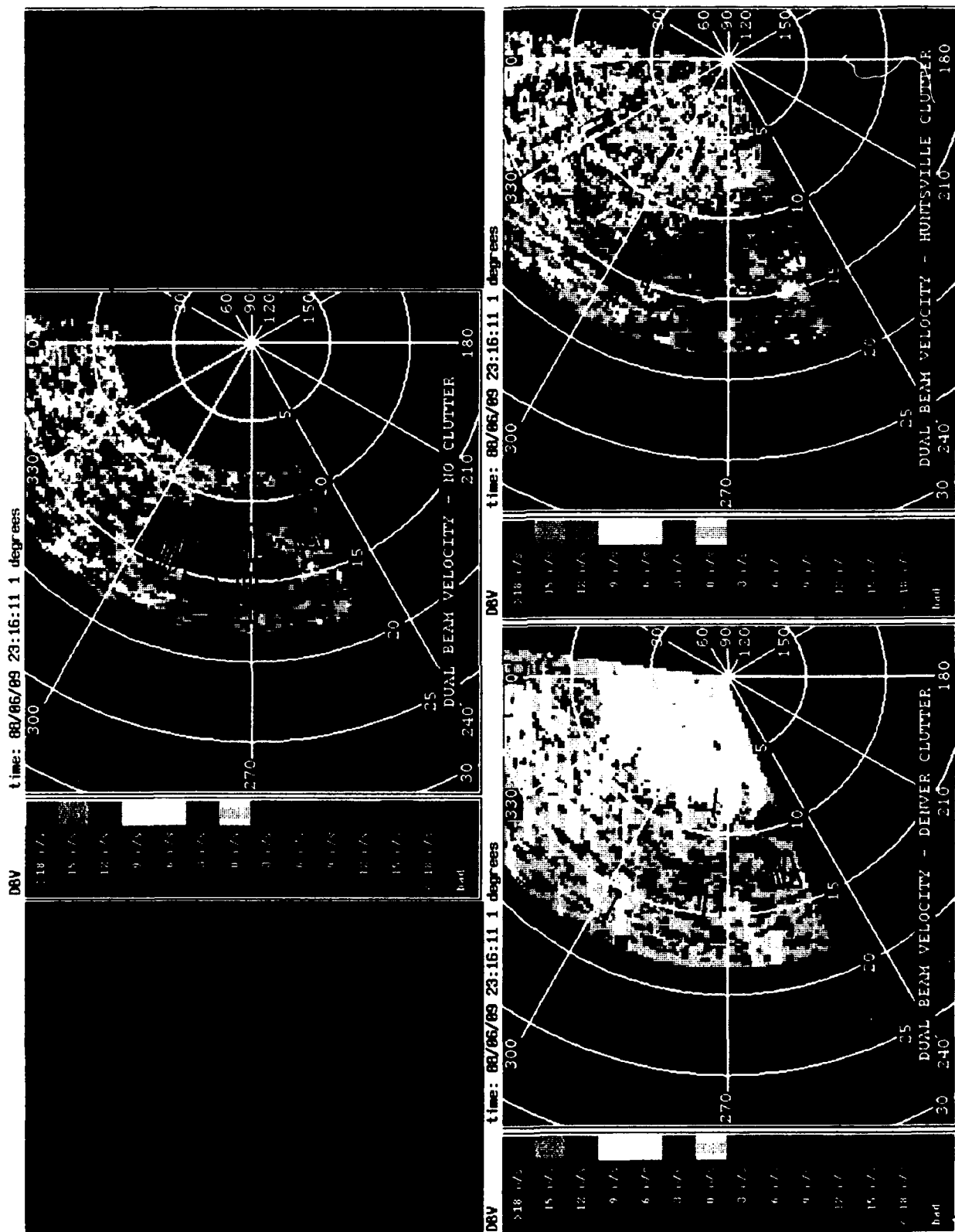


Figure 19. Simulated ASR velocity fields for 22:10 (GMT) June 10, 1988 dry microburst event. Simulations with no clutter, Denver clutter, and Huntsville clutter are shown. Signal-to-noise thresholds are switched off and signal-to-clutter thresholds lowered. Shear segments and associated regions are represented by red lines and red boxes, respectively (range rings at 5 km; azimuth lines every 30 degrees).

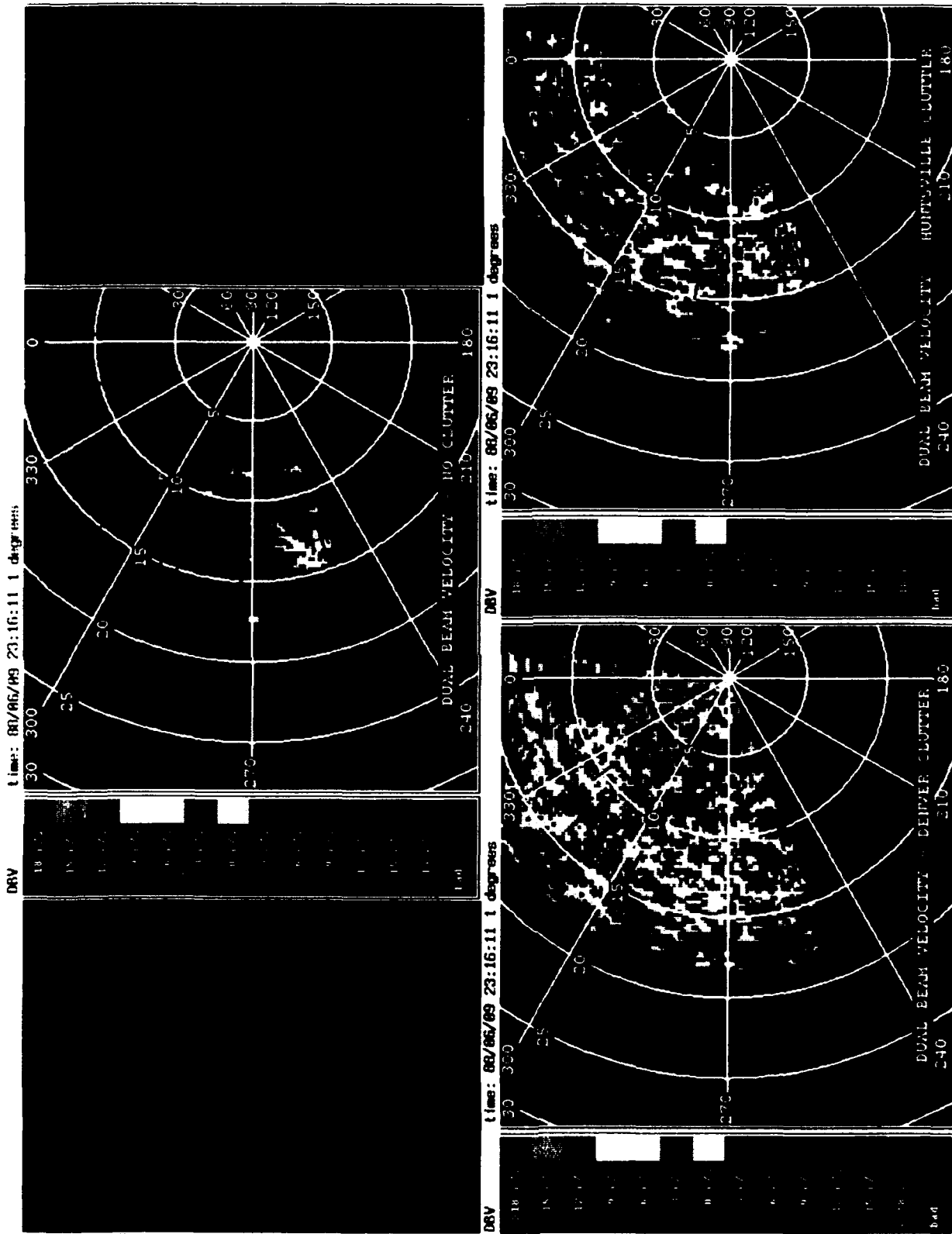


Figure 20. Simulated ASR velocity fields for 22:10 (GMT) June 10, 1988 dry microburst event. Simulations with no clutter, Denver clutter, and Huntsville clutter are shown. Signal-to-noise and signal-to-clutter thresholds are set to default levels. Shear segments and associated regions are represented by red lines and red boxes, respectively (range rings at 5 km; azimuth lines every 30 degrees).

B. EFFECTS OF SIGNAL-TO-NOISE AND OVERHANGING PRECIPITATION ON DRY MICROBURST DETECTION

1. Scoring Results

Table 4 shows the results from applying the ASR microburst detection algorithm to the 11 simulated weather cases containing no clutter contamination. A microburst hit was declared if the algorithm associated shear segments within a kilometer of the microburst in the DBV field.

Table 4.
Scoring Results, Pure Weather (11 Cases)

	Hits			
	One Degree		Two Degree	
Processor Settings	Number	Percent	Number	Percent
Noise Thresholding Off (NTO)	10	91	11	100
Default	8	72	7	64

The table indicates that when signal-to-noise thresholding was switched off, all 11 microbursts with the two-degree tilt and 10 of 11 with the one-degree tilt were detected. This indicates that dry microbursts are detectable in the absence of ground clutter. Neither interference from overhanging precipitation nor weak signal strength prevented detection of these events.

2. Velocity Estimates

Table 5 compares ASR velocity differential estimates to those from the TDWR testbed on the 11 simulated microburst cases containing no clutter. Both human and algorithmic truth comparisons are presented. Human truth estimates, produced by meteorologists estimating the shear from the FL-2 data, tended to be higher than algorithmic truth, which was produced by applying the microburst detection algorithm on the surface FL-2 velocity fields.

On average, the ASR differential velocity estimates are 3-4 m/sec (10-15 percent) lower than the corresponding measurements from the TDWR testbed. In most cases, this is caused by interference from reflectivity aloft. First, since the dual-beam estimator used here can be viewed as an extrapolation of surface velocity from high- and low-beam velocity estimates, enhanced interference from reflectivity aloft in the low beam can still bias estimates downwards. Second, in the simulated dry microbursts, while descending

Table 5.
Microburst Detection Algorithm Velocity Estimator
Performance for Simulated ASR-based Dry Microburst
Velocity Fields Generated Using Dual-Beam
Autocorrelation Method

Beam Elevation	Two-Degree		One-Degree	
Truth Type	Human	Algorithmic	Human	Algorithmic
ΔV_R Bias (m/s)	-3.98	-2.88	-3.56	-2.46
Relative ΔV_R Bias	-0.15	-0.11	-0.14	-0.10
RMS ΔV_R Discrepancy (m/s)	5.61	3.98	5.94	4.22
RMS Relative ΔV_R Discrepancy	0.22	0.16	0.23	0.17

precipitation was adequate to resolve the centers of regions of shear, much lower reflectivities were associated with the outer fringes of the outflow region. Interference from reflectivity aloft biased or overwhelmed surface velocities in these fringes. Shear segments were shortened, driving the resultant velocity estimates downward.

Nevertheless, the velocity estimator's performance statistics in Table 5 are comparable to results of field measurements of wet microbursts made in Huntsville, AL and Kansas City by FL-3. Thus, regardless of the cause of the biases, these velocity statistics should be viewed as a positive result.

C. EFFECTS OF CLUTTER RESIDUE ON DRY MICROBURST DETECTION

This section describes the results when simulated ground clutter time-series was added to the simulated dry microburst time-series

1. Scoring Results

Table 6 shows microburst detection results when the Denver and Huntsville ground clutter were added to the scans analyzed. Ground clutter filtering, as described in Weber (1987), was performed before estimating velocities. As in Table 4, the results shown are from scoring from the dual-beam velocity (DBV) field.

If scoring is expanded so that a detection in either the LBV or DBV fields constitutes a hit, one additional hit is obtained for the Denver two-degree data. Since the dual beam product is still under development, it is hoped that an improved dual-beam velocity estimator will enable the LBV hits to be detectable from the DBV field also.

Table 6.
Weather Plus Clutter Scoring Results (11 Cases - DBV)

		Hits			
		One-Degree Elevation		Two-Degree Elevation	
Clutter	Processor Settings	Number	Percent	Number	Percent
Denver	Normal	5	45	4	36
	Noise Thresholding Off (NTO)	7	64	6	65
Huntsville	Normal	2	18	4	36
	NTO	2	18	5	45

Since all of the events were detectable in the absence of ground clutter (see previous section), missed detections in Table 6 must be the result of ground clutter residue. Further analysis of the cases showed the following:

1. In cases where the clutter-to-signal ratio was less than 20 dB, the microbursts were detected.
2. In cases where the clutter-to-signal ratio was on the order of 20 dB, misses were due to a clutter residue disruption of the continuity of radial shear in the outflow region, resulting in a loss of one or more shear segments. The remaining segments then failed the azimuthal continuity requirements of the microburst detection algorithm.
3. In the cases where the clutter-to-signal ratio was much greater than 20 dB, the entire shear signature was rendered indistinguishable, even to human analysts, and the algorithm failed completely.

These trends are graphically depicted in Figure 21; the algorithmic hits and misses as a function of clutter intensity and weather reflectivity are plotted. The results presented are those of the simulations run with beam nose set at two degrees, with no signal-to-noise thresholding and DBV/LBV scoring. Both Huntsville and Denver ground clutter results are plotted.

The effective clutter reflectivity, plotted on the x-axis, was computed by taking the median clutter cross-section (σ^0) within a 2 km radius of the event's reported center, then converting that value from σ^0 to effective clutter reflectivity, Z_{eff} . The weather reflectivity, plotted on the y-axis, is the maximum surface weather reflectivity in the outflow region as measured by the pencil-beam truth radar.

It is clear from Figure 21 that the hits and misses can be separated into distinct hit and miss regions. In regions of high signal-to-noise (i.e., reflectivity exceeding 0 dBZ in the simulations), it is reasonable to assume that the boundary delimiting the two regions is a straight line of slope one. An appropriate placement of this line is shown in Figure 21.

A conclusion drawn from the figure is as follows: using the current signal processing strategies and microburst detection algorithms, events which occur in regions where the effective clutter exceeds weather reflectivity by 17-20 dB are missed by the current algorithms. Conversely, events which occur in clutter regions where the difference between clutter and weather reflectivities is less than 17 dB are detectable.

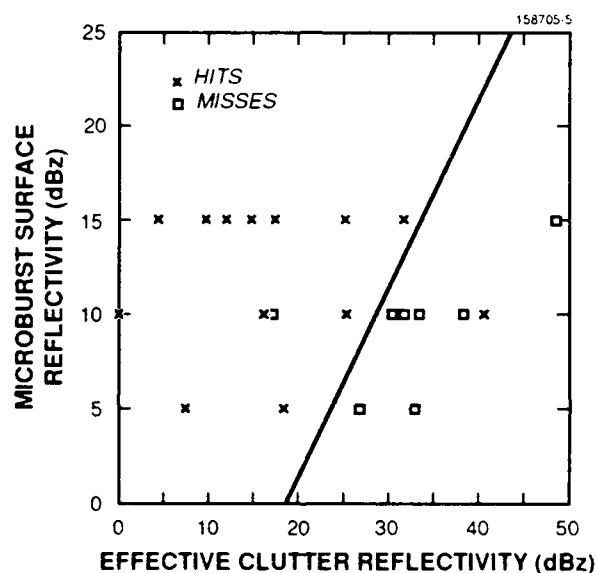


Figure 21. Algorithmic hits (Xs) and misses (boxes) from LBV and DBV fields with adjusted signal-to-noise and signal-to-clutter thresholds plotted on a graph of effective clutter reflectivity versus weather reflectivity.

2. Statistical Analysis

From the results described in the preceding section, an estimate of an ASR's overall probability of detection for microbursts at a particular site can be developed. Specifically, given both weather reflectivity distribution statistics for microburst events occurring in the radar site's environment and the distribution of the site's effective ground clutter reflectivity, the percentage of microburst events missed on account of ground clutter can be predicted.

Figure 22 shows the distribution of reflectivities for microburst events at Denver, measured by the FL-2 radar in 1987 and 1988 between the months of May and September. Note that this histogram includes wet as well as dry microbursts. Forty-one percent of these Denver events were associated with reflectivities of 30 dBZ or less, classifying them as dry.

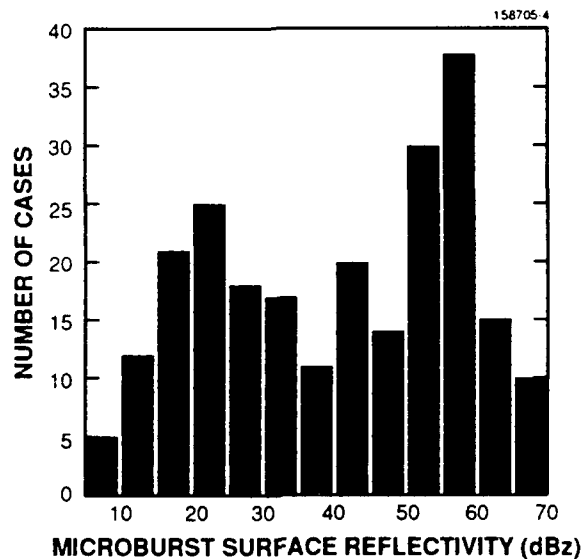


Figure 22. Histogram of microburst surface reflectivity for Denver microburst events exceeding 20 meters per second. Data was taken from FL-2 Denver experiments from May to September 1987 and 1988.

Figure 23a shows the distribution of effective ground clutter reflectivities as seen by an ASR within 15 km of the radar for Denver. Coordinate translation and scaling of the clear day clutter data taken from the FL-2 pencil-beam site was described in Section 2.C. The effective clutter reflectivity distribution was computed as follows: median effective clutter reflectivity within a one-km radius was computed every kilometer out to 15 kilometers, and over all 256 1.4-degree sectors.

This result is extremely sensitive to site selection. Figure 23b shows the ground clutter distribution generated from data taken directly from FL-3 fan-beam testbed site in Huntsville, Alabama. Comparing this distribution to that of Figure 23a, it is apparent that the Huntsville system was sited in a harsher clutter environment. Using this distribution in equation (1) with the Denver microburst distribution, the predicted percentage of total missed detections is now 16 percent, approximately 8 percent worse than with the Denver site's clutter distribution.

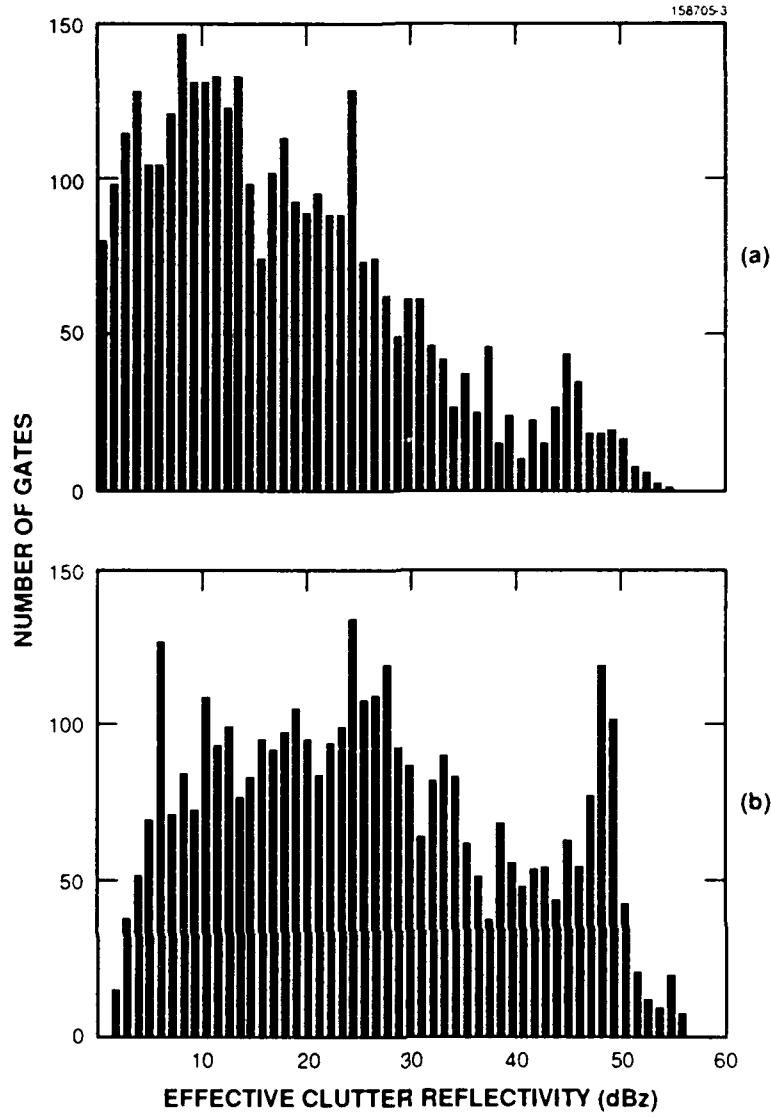


Figure 23. Histograms of clutter intensity (in units of effective clutter reflectivity) for: a) Denver and b) Huntsville for range interval 0-15 km. Both distributions were computed from the clear day clutter maps used in the simulations and described in the text.

Using the two distributions above, the following equation can be evaluated:

$$PercHits = \frac{\int \int f(dBZ_w, dBZ_c) P_w(dBZ_w) P_c(dBZ_c) \Delta dBZ_c \Delta dBZ_w}{\int \int P_w(dBZ_w) P_c(dBZ_c) \Delta dBZ_c \Delta dBZ_w} \quad (1)$$

where

$PercHits \equiv$ Percentage of detectable microburst events

$dBZ_w \equiv$ Weather reflectivity

$dBZ_c \equiv$ Effective clutter reflectivity

$P_w(\text{dBZ}_w) \equiv$ Probability that a microburst will have reflectivity in interval $(\text{dBZ}_w, \text{dBZ}_w + \Delta \text{dBZ}_w)$

$P_c(\text{dBZ}_c) \equiv$ Probability that the clutter environment will have effective reflectivity in interval $(\text{dBZ}_c, \text{dBZ}_c + \Delta \text{dBZ}_c)$

$f(\text{dBZ}_w, \text{dBZ}_c) = \begin{cases} 1 & \text{if } \text{dBZ}_w \text{ and } \text{dBZ}_c \text{ map into the hit region (see Figure 21)} \\ 0 & \text{otherwise} \end{cases}$

Using the microburst weather reflectivity distribution of Figure 22 to approximate P_w , and the Denver clutter distribution of Figure 23a to approximate P_c , equation (1) was evaluated. The hit-miss function, $f(\text{dBZ}_w, \text{dBZ}_c)$, was modelled as

$$f(\text{dBZ}_w, \text{dBZ}_c) = \begin{cases} 1 & \text{dBZ}_c - \text{dBZ}_w < T \\ 0 & \text{otherwise} \end{cases} \quad (2)$$

where

$T \equiv$ clutter signal threshold

If T is between 18 and 20 dB as is suggested by Figure 21, then by equation (1), the percentage of Denver microbursts missed due to ground clutter interference should be 8 percent.

It must be stressed that this method does not predict a total detection probability, only the percentage of detections eliminated through ground clutter interference. Other factors, such as microburst asymmetry, are not included in the computation. However, based on the analysis in this report, ground clutter interference should be the dominant cause of missed microburst detections, so this prediction is significant.

D. FALSE ALARMS AND OTHER ISSUES

1. Scoring

While the simulation procedure was not specifically designed to assess false alarm rates, analysis of the false associations occurring in the simulated cases provides some useful observations, applicable not only to dry events but also to ASR detection of microbursts in general.

Specifically, the processed data contained numerous false associations. Table 7 shows false association statistics from the simulated dry microburst cases. Any association of shear segments -- clusters -- not associated with a shear region in the original FL-2 horizon scan used in the simulation were counted as false. Multiple false clusters occurring in a single scan were counted as a single false association in this scoring. In all cases except the two-degree tilt with Huntsville clutter and default thresholding, false associations occurred between 18 and 45 percent of the time. Although, the two-degree Huntsville cases with default thresholding produced no false

associations, this result should not be viewed optimistically, as Table 6 shows the detection rate in that regime was less than 20 percent.

2. Overhanging Precipitation and the Dual-Beam Product

Overhanging precipitation was the dominant source of false associations in four of the 11 cases. The two June 10, 1988 cases, discussed in sections A.3-4 of this chapter, are typical examples. Markedly different wind direction for near-surface winds versus winds in the higher reflectivity anvil resulted in velocity estimates that approached the velocity of the winds aloft. This study has shown that the subsequent false velocity estimates do not appear to be present in the region of the microburst center, where enough precipitation exists to counteract the vertical shear. However, the false estimates led to many false associations outside the shear region. This effect is not isolated to dry microbursts and has been observed in wet microburst conditions by the FL-3 system in Kansas City in 1989, as well. Efforts are underway to evaluate alternate velocity estimators that may reduce the frequency of false-alarm occurrence.

The June 10, 1988 case studies discussed earlier demonstrated that the default signal-to-noise and signal-to-clutter thresholds do not suffice to eliminate the observed false associations caused by overhanging precipitation. Recall, in the first case, that the thresholds failed to have an appreciable effect on the false associations. In the second case, the thresholds succeeded in filtering out the false associations but eliminated the valid detections as well. So while a few false associations were eliminated through this thresholding, not all were, and valid detections were lost through the same mechanisms that eliminated the false associations. For two reasons, these results were not entirely unexpected. First, the default thresholds were designed to eliminate false alarms due to noise and ground clutter interference, not false alarms resulting from overhanging precipitation. Second, the default thresholds were not optimized for dry microburst detection.

Table 7.
False Association Scoring Results (11 Cases)

		False Associations			
		One-Degree		Two-Degree	
Clutter	Processor Settings	Number	Percent	Number	Percent
None	Default	3	27	0	0
	Noise Thresholding Off (NTO)	5	45	4	36
Denver	Default	2	18	2	18
	NTO	2	18	2	18
Huntsville	Default	3	27	0	0
	NTO	2	18	4	36

A number of other methods may be applied to rid the signal of false alarms. Time association, which is used in the current detection algorithms, may filter many false associations, and nothing indicates that the technique would inhibit dry microburst detection. However, another false alarm rejection technique, reflectivity thresholding, will most likely reject more than false alarms. Reflectivity thresholding eliminates alarms not associated with higher reflectivity convective storm cells. Dry microbursts frequently fall out of the anvil structure (instead of the parent cells) of convective storms. As a result, a dry microburst's reflectivity structure is often fragmented; its radar signature does not often resemble a wet convective storm core, and thus is difficult to distinguish from other low-reflectivity precipitation. While reflectivity thresholding is an important technique being considered for eliminating false alarms in general its use is expected to be incompatible with dry microburst detection.

4. CONCLUSION

Results from the simulation of 11 dry microbursts, with and without ground clutter contamination were presented. It was shown that neither radar sensitivity nor interference from overhanging precipitation prohibited detections of dry microbursts with shear strengths in excess of 20 m/sec. Ground clutter tended to cause missed detections only when median ground clutter reflectivity in the microburst event region exceeds the microburst's surface outflow reflectivity by greater than 17-20 dB.

These observations were used to develop a predictor of ASR microburst detection performance at a particular site for events lost on account of interference by ground clutter residue. In the simulations, this was the predominant cause of missed detections. When computed for Denver's Stapleton ASR, a missed detection rate of slightly less than 10 percent was predicted. If all non-clutter-related causes of missed detections are negligible, this prediction puts a Denver ASR within the TDWR specification. This result is highly dependent on the ambient clutter environment of the radar's site. When a clutter distribution collected from another radar site was applied, failed detections for Denver microbursts rose to almost 20 percent, worse than allowed by the TDWR specification. Although these results warn that inappropriate siting could be detrimental to adequate dry microburst detection by an ASR, they are promising insofar as they do not preclude it.

The study also pointed out areas where the current microburst detection algorithm may be improved. For example, one event occurring close to the radar was missed because of inadequacies in the microburst detection algorithm's capability for detecting events at very short ranges. This problem is currently being addressed.

Also, the simulation results indicated a number of false alarms caused by interference from overhanging precipitation in regions outside of the main storm downdraft. These are not phenomena associated only with dry microbursts, and thus should be a cause of concern for microburst detection in general. Improvements in the dual beam velocity product should help eliminate many false alarms. Reflectivity thresholding, while it would improve false-alarm rates, would almost certainly degrade the detection of dry microburst events.

REFERENCES

M. Weber and W. Moser, "A preliminary assessment of thunderstorm outflow wind measurement with airport surveillance radars," MIT Lincoln Laboratory, Lexington, MA, Project Report ATC-140 (May, 1987).

M. Weber, "Ground clutter processing for wind measurements with airport surveillance radars," MIT Lincoln Laboratory, Lexington, MA, Project Report ATC-143 (November, 1987).

D. Sirmans, and W. Bumgarner, "Numerical comparison of five mean frequency estimators," *J. of Appl. Meteorol.*, vol. 14, pp. 991-1003 (September, 1975).

M. Weber, and T. Noyes, "Low-altitude wind shear detection with airport surveillance radars: evaluation of 1987 field measurements," MIT Lincoln Laboratory, Lexington, MA, Project Report ATC-159, (August, 1988).

M. Weber, "Dual-beam autocorrelation based wind estimates from airport surveillance radars," MIT Lincoln Laboratory, Lexington, MA, Project Report ATC-167, (June, 1989).

APPENDIX A SYNTHESIS OF RHIs FROM PPI VOLUME SCAN DATA

This appendix describes the procedure used in generating interpolated RHIs from PPI data. At each range gate, a two-dimensional grid is set up in θ - ϕ (azimuth-elevation) space. The PPI product data is laid onto the appropriate elevations. The weather product value for each unfilled grid point \hat{A} is estimated from all N filled neighboring product values by computing the weighted average

$$\hat{A} = \frac{\sum_{n=0}^N W_n A_n}{\sum_{n=0}^N W_n}$$

W_n is a Cressman weighting; it is a function of s_n , the distance from the unfilled grid point to the filled neighboring grid point, where the product value is A_n .

$$W_n = \begin{cases} \left(\frac{s_0^2 - s_n^2}{s_0^2 + s_n^2} \right)^\alpha & \text{if } s_n \leq s_0 \\ 0 & \text{if } s_n > s_0 \end{cases}$$

where

$s_0 \equiv$ Cressman distance parameter (degrees)

$\alpha \equiv$ Cressman exponent parameter

The angular distance s_n is computed

$$s_n^2 = \theta_n^2 + \phi_n^2$$

where

$\phi_n \equiv$ elevation separation (degrees)

$\theta_n \equiv$ azimuthal separation (degrees)

Figure A-1 plots the Cressman weight W versus relative distance $\frac{s}{s_0}$ for four values of α . As illustrated in the graph, a higher alpha increases the relative weighting of nearby grid points. The Cressman distance parameter s_0 defines the maximum range for the interpolation. For the synthesis of RHIs from PPIs, settings of $\alpha = 4$ and $s_0 = 10^\circ$ were found to provide realistic interpolated storm profiles where elevation separation between PPIs was a few degrees or less.

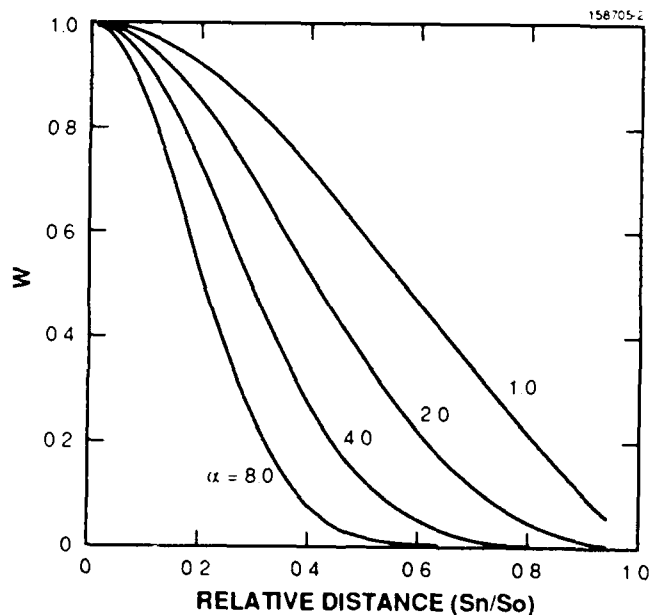


Figure A-1. Cressman weight versus relative distance for four values of α .

However, this weighting scheme produced unrealistic estimates for values at grid points where the gap between PPIs exceeded five degrees. It was desired that less weight be placed on grid points azimuthally separated from the unknown value. This correction was implemented by applying a skewing factor k . A skewed distance s'_n was calculated and used in place of s_n in Equation A-1. s'_n was computed as follows

$$s'^2_n = k \theta^2_n + \phi^2_n$$

where

$$k \equiv \text{PPI-to-RHI skewed weighting factor}$$

In a normal Cressman weighting, the value of k is one. A high value for k weights elevation proximity much higher than azimuthal proximity. Setting $k = 10$ was empirically found to produce satisfactory interpolated RHI fields from PPIs.